JOURNAL OF PETROLOGY | VOLUME 54 | NUMBER 10 | PAGES 1997–2031 | 2013 | doi:10.1093/petrology/egt039

Strain Localization in Pyroxenite by Reaction-Enhanced Softening in the Shallow Subcontinental Lithospheric Mantle

KÁROLY HIDAS[1]*, CARLOS J. GARRIDO[1], ANDREA TOMMASI[2], JOSÉ ALBERTO PADRÓN-NAVARTA[2,3], MARCEL THIELMANN[4], ZOLTÁN KONC[1], ERWIN FRETS[1] AND CLAUDIO MARCHESI[1]

[1]INSTITUTO ANDALUZ DE CIENCIAS DE LA TIERRA (IACT), CSIC & UGR, AVENIDA DE LAS PALMERAS 4, 18100 ARMILLA (GRANADA), SPAIN

[2]GÉOSCIENCES MONTPELLIER, UNIVERSITÉ MONTPELLIER 2 & CNRS, CC 60, PLACE E. BATAILLON, 34095 MONTPELLIER, FRANCE

[3]RESEARCH SCHOOL OF EARTH SCIENCES, AUSTRALIAN NATIONAL UNIVERSITY, BUILDING 61, MILLS ROAD, CANBERRA, ACT 0200, AUSTRALIA

[4]INSTITUTE OF GEOPHYSICS, ETH ZÜRICH, SONNEGGSTRASSE 5, NO H25, 8093 ZÜRICH, SWITZERLAND

RECEIVED NOVEMBER 28, 2012; ACCEPTED JUNE 10, 2013
ADVANCE ACCESS PUBLICATION JULY 19, 2013

We report structural evidence of ductile strain localization in mantle pyroxenite from the spinel to plagioclase websterite transition in the Ronda Peridotite (southern Spain). Mapping shows that, in this domain, small-scale shear zones occurring at the base of the lithospheric section are systematically located within thin pyroxenite layers, suggesting that the pyroxenite was locally weaker than the host peridotite. Strain localization is associated with a sudden decrease of grain size and increasing volume fractions of plagioclase and amphibole as a result of a spinel to plagioclase phase transformation reaction during decompression. This reaction also fostered hydrogen extraction ('dehydroxylation') from clinopyroxene producing effective fluid saturation that catalyzed the synkinematic net-transfer reaction. This reaction produced fine-grained olivine and plagioclase, allowing the onset of grain-size sensitive creep and further strain localization in these pyroxenite bands. The strain localization in the pyroxenites is thus explained by their more fertile composition, which allowed earlier onset of the phase transition reactions. Geothermobarometry undertaken on compositionally zoned constituent minerals suggests that this positive feedback between reactions and deformation is associated with cooling from at least 1000°C to 700°C and decompression from 1·0 to 0·5 GPa.

KEY WORDS: *mylonite shear zone; pyroxenite; Ronda Peridotite massif; strain localization; synkinematic reaction*

INTRODUCTION

Rock deformation in response to forces in the Earth's interior is governed by rheology, which varies as a function of constitutive and environmental aspects including mineralogy, fluid content and chemistry, melt fraction, temperature, pressure, differential stress conditions, and grain size. Studies of mantle xenoliths, orogenic peridotites, and ophiolites indicate that plastic deformation of the shallow lithospheric mantle is mostly accommodated by dislocation creep mechanisms [for a review see Vauchez *et al.* (2012)]. However, microstructural studies on fine- and ultrafine-grained mylonites in shear zones indicate that grain-size sensitive creep processes may also accommodate significant strain in localized zones during thinning and exhumation of the shallowest lithospheric mantle (Kirby, 1985; Boudier *et al.*, 1988; Drury *et al.*, 1991; Jaroslow *et al.*, 1996; Jin *et al.*, 1998; Warren & Hirth, 2006;

*Corresponding author. Telephone: 0036 70 2442095. E-mail: karoly.hidas@csic.es

Skemer *et al.*, 2010; Kaczmarek & Tommasi, 2011; Vauchez *et al.*, 2012). Syn-deformational dynamic recrystallization (Warren & Hirth, 2006; Precigout *et al.*, 2007; Karato, 2008) or reactions accompanying the deformation (Brodie, 1980; Drury *et al.*, 1991; Jin *et al.*, 1998; Furusho & Kanagawa, 1999; Newman *et al.*, 1999; Kaczmarek & Tommasi, 2011) are among the proposed mechanisms for producing fine-grained peridotites in which strain localizes. Synkinematic net-transfer metamorphic reactions can both result in fine-grained reaction products and promote a positive feedback between deformation and reaction (Furusho & Kanagawa, 1999; Newman *et al.*, 1999). A particularly relevant reaction in the exhumation and thinning of the lithosphere is the spinel to plagioclase phase transformation reaction (Furusho & Kanagawa, 1999; Newman *et al.*, 1999; Kaczmarek & Tommasi, 2011), which occurs at relatively shallow depths in the lithospheric mantle (e.g. Herzberg, 1972; Presnall, 1976; Borghini *et al.*, 2010, 2011). Experimental studies show that this phase transformation reaction is shifted towards higher pressure in fertile (i.e. clinopyroxene-rich) whole-rock compositions (Borghini *et al.*, 2010). In a mantle section composed of peridotites and pyroxenites, this reaction will thus occur at greater depths in the pyroxenites. Therefore, in the waning stages of exhumation of the subcontinental lithospheric mantle in extensional settings, the locus and extent of strain localization may strongly depend on the distribution of tabular pyroxenite bodies.

Structural mapping in the southwestern part of the Ronda Peridotite massif in southern Spain highlights that shear zones located in the transition between the spinel and the plagioclase lherzolite domains are systematically developed in plagioclase–spinel pyroxenites, indicating that these pyroxenites were weaker than the surrounding peridotite. These centimeter- to decimeter-scale pyroxenite mylonite zones occur at the tips of larger (10–15 m wide) shear zones that formed during kilometer-scale folding and shearing of the attenuated subcontinental lithospheric mantle, which accommodated the emplacement of the massif in the crust (Hidas *et al.*, 2013). In this paper we present a detailed microstructural and petrological study of one of these mylonitic zones associated with plagioclase–spinel pyroxenites, aiming to unravel potential processes allowing for strain localization in the shallow lithospheric mantle.

DEFORMATION AND STRAIN LOCALIZATION IN THE RONDA PERIDOTITE

The Ronda massif is a section of the subcontinental lithospheric mantle emplaced in the internal domains of the Betic Cordillera. In its western part, this massif is zoned into four kilometer-scale domains (garnet–spinel mylonite, spinel tectonite, granular spinel peridotite, and plagioclase tectonite domains), which display structures and metamorphic assemblages frozen at different stages of the tectono-metamorphic evolution during exhumation (Obata, 1980; Van der Wal & Bodinier, 1996; Van der Wal & Vissers, 1996; Garrido & Bodinier, 1999; Lenoir *et al.*, 2001; Precigout *et al.*, 2007; Soustelle *et al.*, 2009; Hidas *et al.*, 2013) (Fig. 1). Shear zones, defined by fine-grained peridotite mylonites, occur both in the garnet–spinel mylonite (Van der Wal & Vissers, 1996; Precigout *et al.*, 2007; Soustelle *et al.*, 2009; Garrido *et al.*, 2011) and in the plagioclase tectonite domains (Hidas *et al.*, 2013), which are located respectively at the top and bottom of the mantle section exposed in this massif (Fig. 1). These shear zones record different stages of the evolution of the massif. The garnet–spinel mylonite domain accommodated exhumation and cooling of garnet peridotites from 2·4–2·7 GPa at 1020–1100°C (*c.* 85 km) to 2 GPa at 800–900°C (*c.* 65 km) as a result of early thinning of the Alborán Domain in the Oligocene (Precigout *et al.*, 2007; Garrido *et al.*, 2011). Plagioclase tectonites formed during kilometer-scale folding of an attenuated lithospheric mantle upon decompression from spinel to plagioclase lherzolite facies prior to the emplacement into the crust in the Late Oligocene–Early Miocene, as described by Hidas *et al.* (2013). According to those researchers, the earliest shear zones that formed during this event occur at the transition from the granular spinel peridotite to the plagioclase tectonite domain (inset in Fig. 1). In this part of the massif, centimeter- to decimeter-wide mylonitic or even ultramylonitic bands are associated with plagioclase-bearing spinel pyroxenite layers (Fig. 1a–d). These bands accommodate shearing parallel to the trend of the (ultra)mylonite bands as denoted by the rotation of the foliation, which is marked by the shape-preferred orientation of porphyroclasts, at their contact (see Fig. 1d). These small-scale shear zones have foliations steeply dipping to the NNW.

For this study we chose an outcrop that corresponds to one of the first occurrences of plagioclase-bearing spinel pyroxenite mylonitic zones down section from the transition between the granular spinel peridotite and plagioclase tectonite domains (Fig. 1). These mylonites exhibit a well-developed foliation dipping steeply to the north (60/355; inset in Fig. 1b), subparallel to the trend of the host pyroxenite layer. The mylonitic foliation crosscuts the higher temperature, westward dipping foliation of the surrounding spinel peridotites (85/280; inset in Fig. 1b). The pyroxenite mylonites have also a NE–SW- trending (N25E–N50E) lineation in the foliation plane marked by elongated pyroxene porphyroclasts and spinel. Sigmoidal pyroxene porphyroclasts and elongate spinel at the contact between the mylonite shear zone and the adjacent coarse-grained host pyroxenite (see Figs 1d, 2c and 3e) indicate a top-to-the-south or -SW sense of shear.

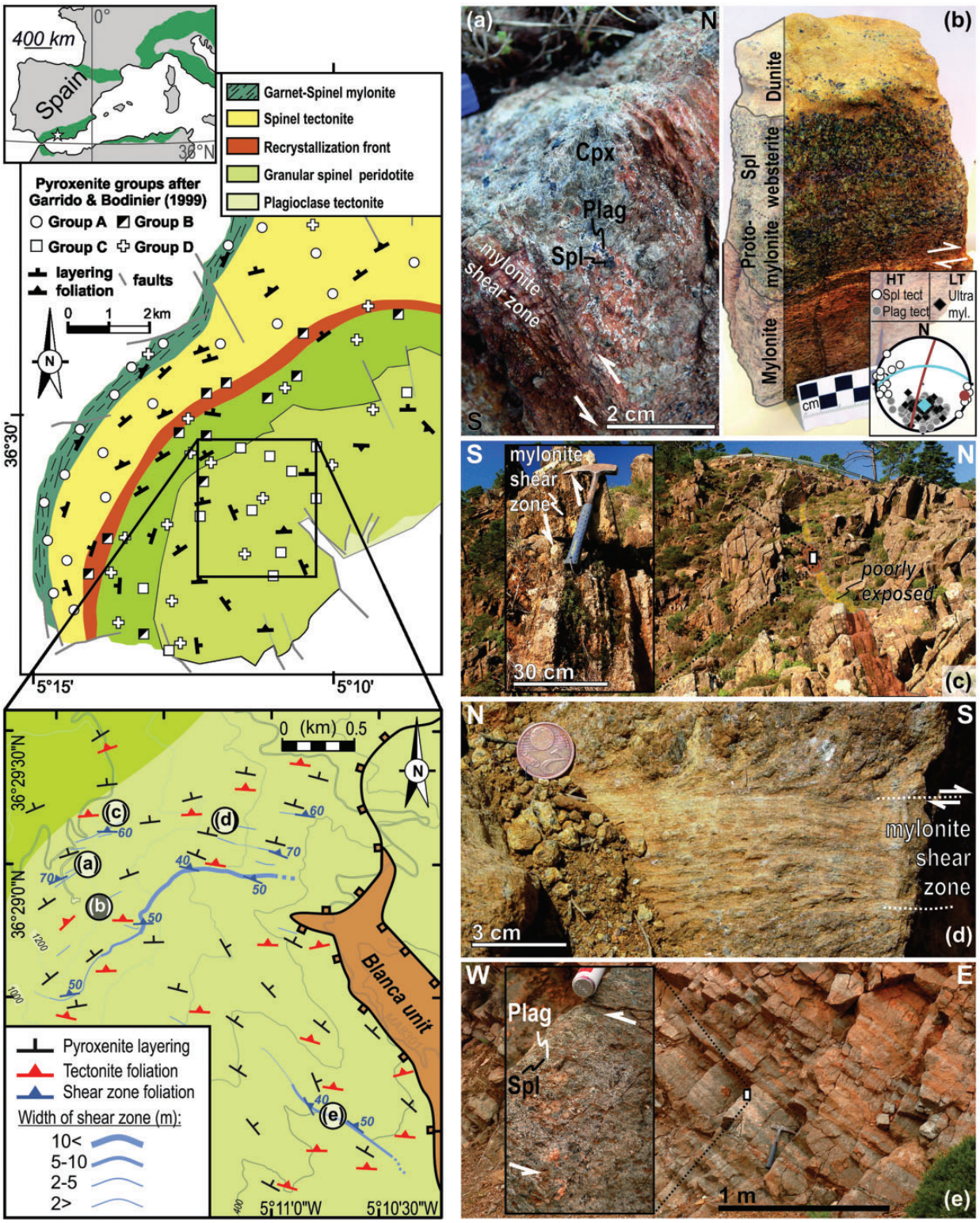

Fig. 1. Schematic structural map and tectono-metamorphic domains of the Ronda Peridotite (after Darot, 1973; Obata, 1980; Van der Wal & Vissers, 1996; Lenoir *et al.*, 2001; Precigout *et al.*, 2007; Soustelle *et al.*, 2009; Hidas *et al.*, 2013). From older to younger structures and from the top to the bottom (from NNW to SSE), the massif is composed of the following units: (1) garnet–spinel mylonite; (2) spinel tectonite; (3) granular spinel peridotite; (4) underlying plagioclase tectonite domains. The transition from the spinel tectonite to the granular spinel peridotite domain is a narrow (*c.* 200–400 m wide) and continuous (*c.* 20 km long) transitional zone referred to as the recrystallization front, which is

(continued)

Further down section, within the plagioclase tectonite domain that constitutes the bottom of the lithospheric section to the SSE of the massif, pyroxenite mylonite shear zones become wider (up to meter scale, Fig. 1e) and the strike of their foliation rotates clockwise, dipping moderately to the NNE (inset in Fig. 1). Although the continuity of pyroxenite shear zones highly depends on the exposure of outcrops, in some cases shear zones can be tracked for several dozens of meters or even 100 m (Fig. 2c). It is noteworthy that the widening of mylonite shear zones towards the base of the massif is accompanied by a switch in shear zone lithology. Although at the transition between the granular spinel peridotite and the plagioclase tectonite domains (study area) mylonites are dominantly hosted in plagioclase-bearing pyroxenites, shearing in the underlying plagioclase tectonite domain is mostly accommodated in peridotites. Both types of shear zones have the same kinematics as indicated by their subparallel foliations and lineations and same shear sense.

SAMPLING AND MICROSTRUCTURAL ANALYSIS METHODS

We studied in detail a 50 cm long section containing a 15 cm wide plagioclase-bearing spinel pyroxenite (olivine websterite) layer that is hosted in coarse-grained dunite and contains a single, fine-grained mylonite zone in its center (Fig. 1b). The studied pyroxenite mylonitic zone (Fig. 1b) has been selected based on geometric considerations, as it is neither too thin (Fig. 1a) nor too thick (Fig. 1e) for detailed microstructural investigation. Other mylonite zones in this part of the massif reflect similar symmetric or asymmetric microstructural zoning. On the basis of lithological and textural differences (Figs 1–4), we defined four microstructural zones: (1) the porphyroclastic dunite that encloses the pyroxenite layer; (2) a coarse-grained Spl websterite in contact with dunite, which lacks plagioclase; (3) a Spl–Plag websterite with a porphyroclastic texture, which is a protomylonite [following the classification of Sibson (1977)]; (4) a Plag–Spl websterite mylonite that occurs as a fine-grained zone in the middle of the pyroxenite layer. For each zone, oriented thin sections were cut perpendicular to the foliation of the mylonite shear zone and parallel to the lineation (*xz* thin sections). The macroscopic foliation and lineation were evident only in the mylonite; consequently, all pole figures in Fig. 5 are presented in the latter structural framework.

Crystallographic preferred orientation (CPO) of minerals in all zones were measured by indexing of electron backscattered diffraction (EBSD) patterns using the JEOL JSM 5600 SEM-EBSD facility of the Géosciences Montpellier (University of Montpellier-2, France). For each sample, we obtained CPO maps covering most of the thin section surface with a grid step of 35–70 μm, depending on the average grain size (a grid step of 15 μm was used for a detailed map in RK139-06). In addition, in three thin sections from the mylonite, six high-resolution crystal orientation maps with step sizes ranging from 0·3 to 1 μm were obtained using the CamScan Crystal Probe X500-FEG SEM–EBSD system of the Géosciences Montpellier (University of Montpellier 2, France). All the major phases in the rocks (olivine, enstatite, diopside, chromite, labradorite, and pargasite) were indexed, and the percentage of indexed points in all raw CPO maps exceeds 70%. EBSD data were processed using the CHANNEL5 software package from Oxford Instruments HKL. Post-acquisition data processing was used to increase the indexing rate by (1) filling the non-indexed pixels that have up to eight identical neighbors with the same orientation and repeating this operation using seven, six and five identical neighbors,

Fig. 1 Continued
considered as a former isotherm overlying partially molten granular peridotites (Van der Wal & Bodinier, 1996; Lenoir *et al.*, 2001). The crustal Blanca Unit has a tectonic contact underlying the Ronda Massif. The study area is shown in detail in the inset, and (a)–(e) show representative structures observed in the field. The term foliation refers to those penetrative planar structural features in the rock that are formed as a result of ductile deformation in contrast to compositional layering represented mainly by pyroxenites. We distinguish high-temperature tectonite foliation that is observed in deformed peridotite host rock and lower-temperature shear zone foliation that occurs within localized mylonitic peridotite, or pyroxenite shear zones. Small numbers on shear zone foliation indicate the dip values where, for example, 60 should be read as a 60° dip. It should be noted that (a), (b), (c), (d) and (e) in the inset refer to the location of the outcrops shown in (a)–(e), respectively. (a) Strain localization in pyroxenite is illustrated by centimeter-scale pyroxenite mylonites at the spinel to plagioclase facies transition. (b) Localized deformation in a pyroxenite layer hosted in dunite (this study). Inset shows lower hemisphere, equal angle (Wulff) stereographic projection of high-temperature (HT) peridotite foliation (dark red) from the closest tectonite outcrop, and lower-temperature (LT) pyroxenite mylonite foliation (blue) from the studied outcrop as traces of planes and their poles. Poles of foliation in HT spinel tectonite and garnet–spinel mylonite from the overlying Ronda domains (white circles; e.g. Darot, 1973; Obata, 1980; Van der Wal & Vissers, 1996; Lenoir *et al.*, 2001; Precigout *et al.*, 2007; Soustelle *et al.*, 2009), and HT plagioclase tectonite (grey circles) and LT peridotite mylonite (black diamonds) from the underlying plagioclase tectonite domain (Hidas *et al.*, 2013) are also shown for comparison. It should be noted that in the vicinity of the studied outcrop peridotite structures are subparallel to those of the overlying units, whereas the pyroxenite mylonite formed in the same kinematic framework as the underlying HT plagioclase tectonites and LT peridotite mylonites. (c) East–west-trending, 50 cm wide mylonitic shear zone localized in pyroxenite. Inset on the left shows a close-up view of the shear zone; its position is indicated by a white rectangle in the main figure of (c). (d) Sigmoidal pyroxene (and spinel) porphyroclasts at the contact between the coarse-grained pyroxenite and the mylonite shear zone are used as shear-sense indicators. At the bottom of the mantle section exposed in the Ronda Massif, mylonite shear zones, localized either in peridotite or in pyroxenite, indicate top-to-the-south or -SW sense of shear. (e) Several meters-wide mylonite shear zone localized in pyroxenite close to the bottom of the Ronda Peridotite. Inset on the left shows a close-up view of the shear zone; its position is indicated by a white rectangle in the main figure of (e).

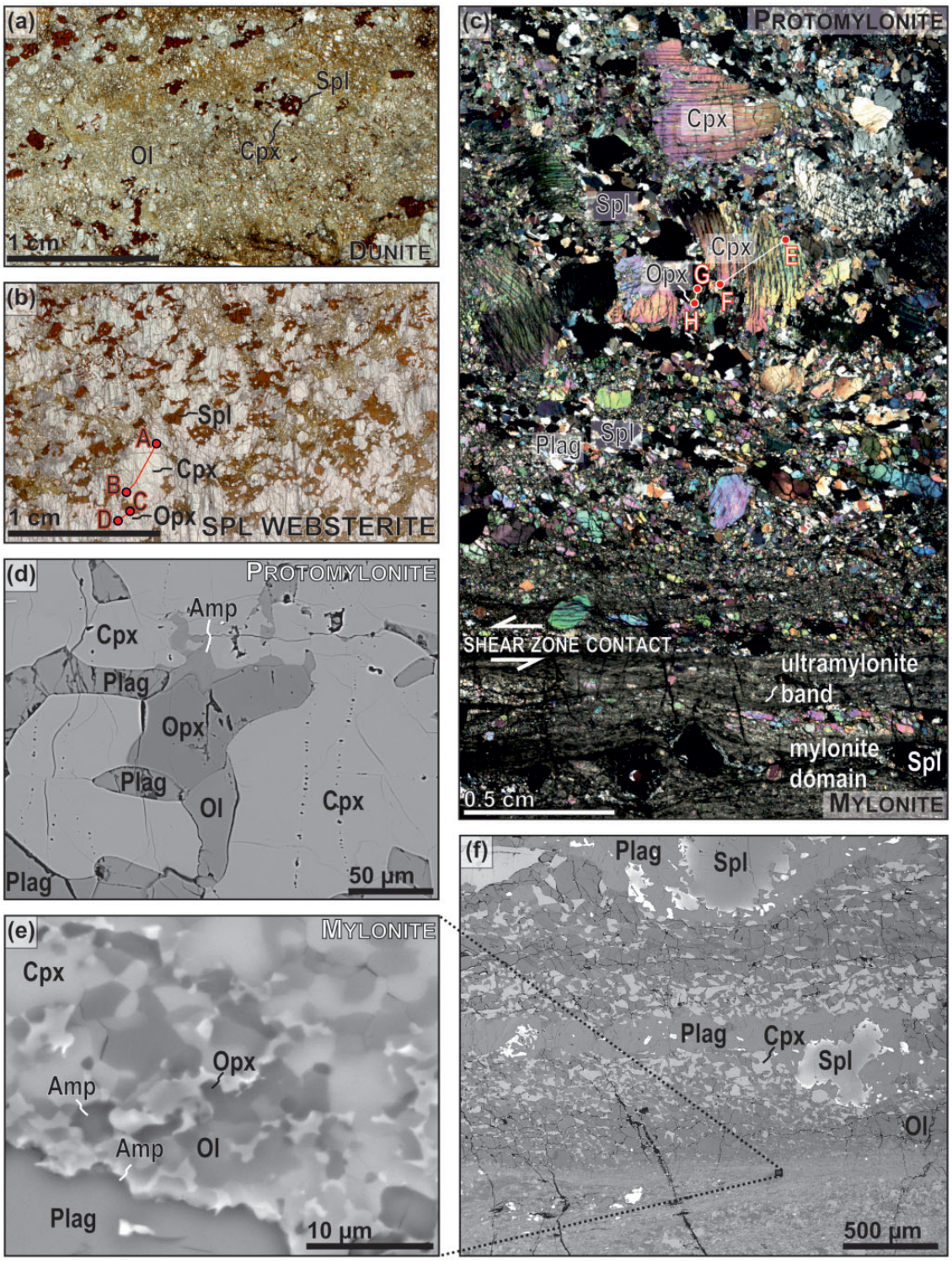

Fig. 2. (a) Coarse-grained fabric of dunite that hosts the pyroxenite layer. Image is taken from a scanned thin section. (b) Coarse-grained, plagioclase-free Spl websterite zone of the studied pyroxenite. A–B and C–D indicate the position of the EPMA mineral profiles shown in Fig. 7. Image is taken from a scanned thin section. (c) Plagioclase-bearing protomylonite (coarse-grained, at top) and the mylonite shear zone (fine-grained, at bottom). E–F and G–H indicate the position of the EPMA mineral profiles shown in Fig. 7. The photomicrograph was taken with crossed polars. (d–f) Back-scattered electron images showing amphibole in the protomylonite as an interstitial phase (d), and replacing the rim of fine-grained plagioclase (e) in an anastomosing ultramylonite band in the mylonite zone (f). Amp, amphibole; Cpx, clinopyroxene; Ol, olivine; Opx, orthopyroxene; Plag, plagioclase; Spl, spinel.

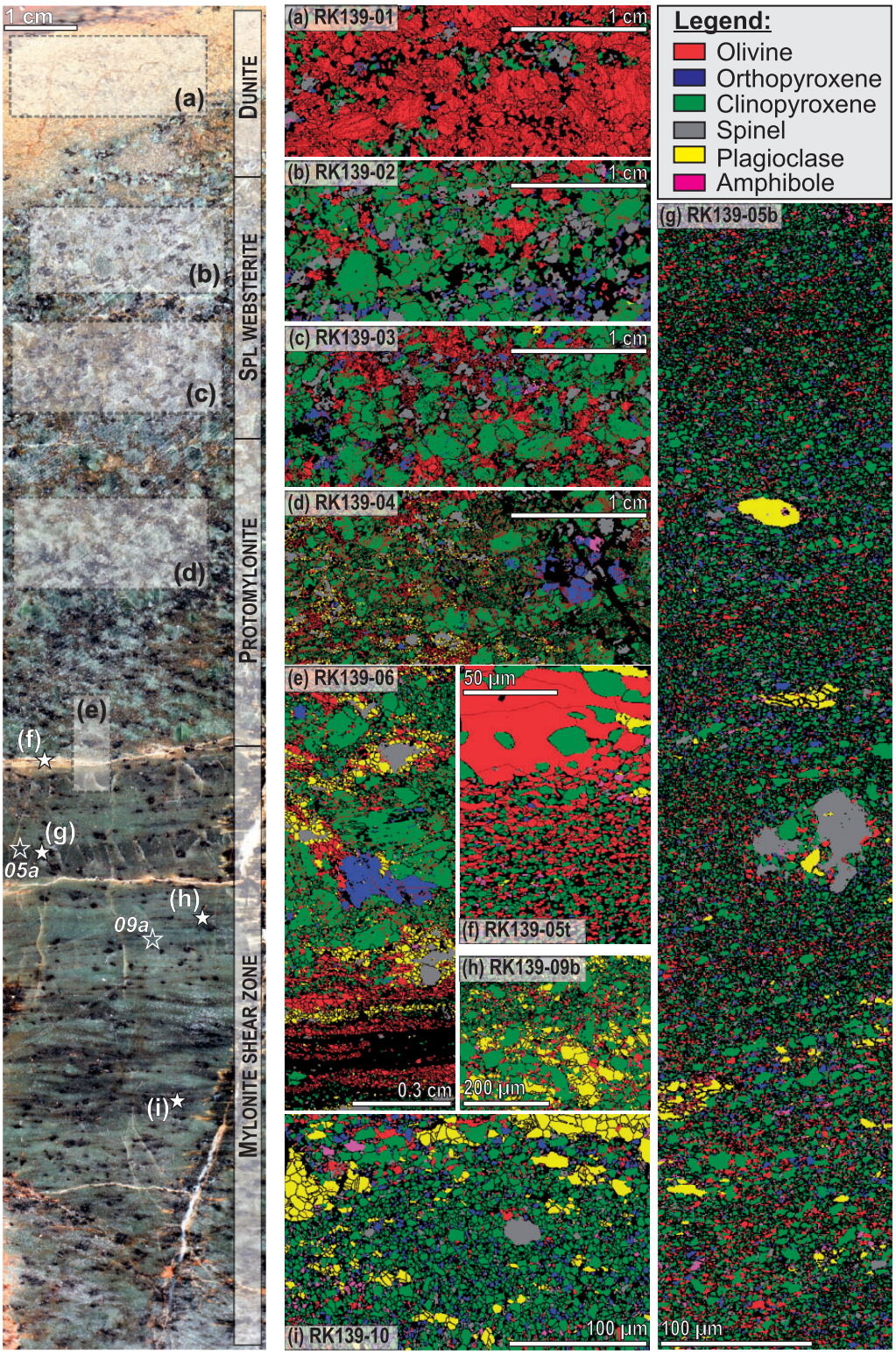

Fig. 3. Macroscopic view and EBSD phase maps of the studied rock slab cut perpendicular to the shear zone foliation and parallel to the mineral lineation. Approximate position of EBSD phase maps (a)–(i) are marked on the photomicrograph. It should be noted that the phase maps of samples 05a and 09a are not shown but their orientation data are used in this study. (a) Dunite zone; (b, c) Spl websterite zone; (d, e) protomylonite zone; (f) protomylonite–mylonite contact; (g, i) ultramylonite bands in the mylonite zone; (h) mylonite subdomain in the mylonite zone.

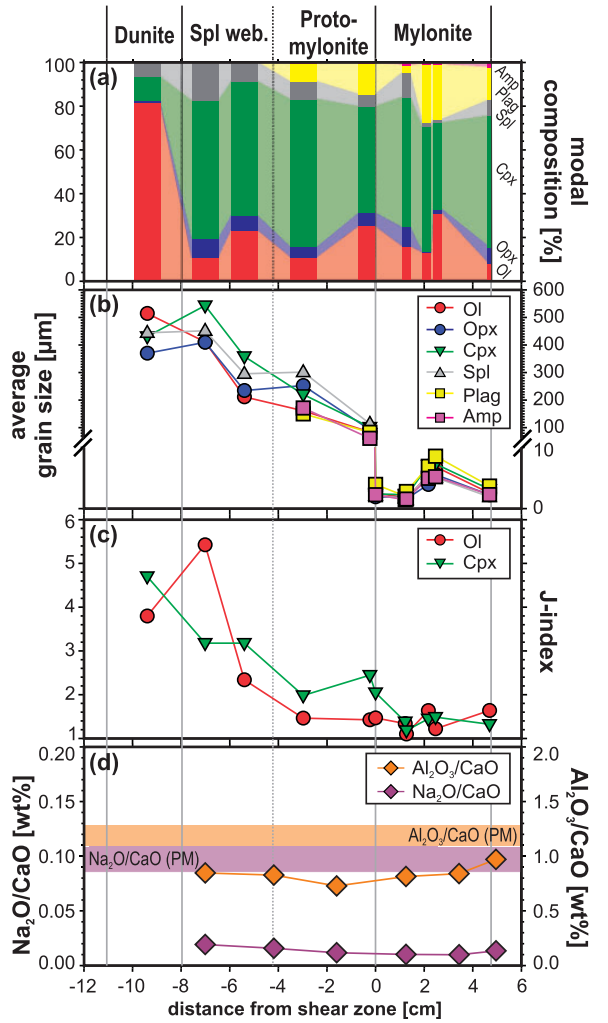

Fig. 4. Modal composition (a), grain size (b), J-index (c), and whole-rock composition (d) across the studied sample, from the dunite (left) to the mylonite shear zone (right). Protomylonite–mylonite contact is at zero. In (a) color coding is the same as in Fig. 3, and wider the vertical bar, larger the area mapped by EBSD at the given microstructural zone. Amp, amphibole; Cpx, clinopyroxene; Ol, olivine; Opx, orthopyroxene; Plag, plagioclase; Spl, spinel. PM in (d) stands for the primitive mantle composition averaged from Hart & Zindler (1986), Falloon & Green (1987), Hirose & Kushiro (1993), Baker & Stolper (1994) and McDonough & Sun (1995). J-index is calculated after Bunge (1982).

(2) identifying the grains as continuous domains characterized by an internal misorientation of $<15^{\circ}$, and (3) correcting olivine misindexing owing to hexagonal pseudosymmetry, resulting in similar diffraction patterns for orientations differing by a rotation of 60° around [100], all steps using the CHANNEL algorithms. Over-extrapolation of data was avoided by comparing with optical micrographs after each step. To avoid over-representation of orientation of large crystals, pole figures are plotted as one measurement per grain (average Euler angles for each grain) using the Unicef careware software package of David Mainprice (ftp://www.gm.univ-montp2.fr/mainprice/CareWare_Unicef_Programs/).

MICROSTRUCTURES

Dunite zone

The dunite (Figs 1b and 4a) has a porphyroclastic texture (Fig. 2a) mainly composed of centimeter-sized olivine accompanied by very minor and smaller-sized (<5 mm) orthopyroxene, clinopyroxene, and spinel (Figs 2a, 3a and 4b). Grain shapes are irregular with slightly curvilinear grain boundaries that locally evolve to polygonal aggregates with 120° triple junctions. Olivine displays, however, a weak shape-preferred orientation (SPO), marking a foliation (Fig. 3a). All minerals display undulose extinction, but olivine also shows widely spaced subgrain boundaries. Core and mantle structures, characterized by fine-grained aggregates surrounding the porphyroclasts (here, olivine) are less common than in the pyroxenites.

Spinel and clinopyroxene are usually clustered in centimeter-long aggregates elongated consistently with the olivine SPO. These aggregates also contain orthopyroxene ± olivine (Fig. 3a). Spinel in thin section is reddish brown in color and forms trails that trend parallel to the maximum elongation direction of the clinopyroxene-rich patches (Fig. 2a).

Granular pyroxenite zones

The Spl websterite zone shows a sharp contact with the dunite and a diffuse transition to the plagioclase-bearing pyroxenite. It is mainly composed of large (maximum 0·5 cm in diameter) irregularly shaped clinopyroxene and spinel (Figs 2b, 3b, c and 4a, b). Olivine can be present as small (200–500 μm) crystals along the boundaries of larger pyroxene grains. Orthopyroxene is rare and has a small grain size (≤400 μm) (Fig. 3b and c). Spinels tend to form trails, which are parallel those observed in the clinopyroxene-rich patches of the dunite. In thin section, they have a reddish brown color at the peridotite–pyroxenite contact that grades into pale green with reddish brown rims away from it (Fig. 2b). Large clinopyroxenes have undulose extinction, embayed grain boundaries, and exhibit twinning and exsolution lamellae of orthopyroxene.

The plagioclase-bearing protomylonite (Fig. 4a) has a porphyroclastic texture (Figs 2c and 4b). Porphyroclasts are mainly pyroxenes (both ortho- and clinopyroxene) with grain sizes similar to those in the Spl websterite, but they are surrounded by smaller, strain-free neoblasts (maximum 200–300 μm in diameter) of the same minerals forming a recrystallized rim (Fig. 3d and e). As in the Spl websterite, undulose extinction, exsolution lamellae, and twinning are common in the pyroxene porphyroclasts. Spinel is pale green in color and always has a metamorphic rim that becomes wider towards the mylonitic zone, composed of small-sized (<200 μm), strain-free plagioclase,

olivine, and amphibole (Fig. 3d and e). Amphibole either replaces clinopyroxene or occurs in the rims around plagioclase, indicating hydration (Fig. 2d). The size of the spinel + plagioclase + olivine ± amphibole aggregates is identical to that of the single spinel crystals in the Spl websterite. In the immediate vicinity of the mylonitic zone, both the pyroxene porphyroclasts with their recrystallized rims and the spinels surrounded by the plagioclase-bearing mineral aggregates show a clear shape-preferred orientation with a maximum elongation oblique by a clockwise rotation of 30–35° to the shear zone trend (Figs 2c and 3e).

Mylonite zone

The mylonite zone is composed of two subdomains, which we refer to as the mylonite and the ultramylonite, and has a sharp contact with the protomylonite zone characterized by an abrupt grain-size reduction (20–50 μm, down to ~10 μm in ultramylonitic bands; Fig. 4b). The mylonite zone is also characterized by the development of a new pervasive foliation parallel to its boundaries (Figs 1b and 2c). Pale green-colored spinel forms large porphyroclasts (up to 2 mm in size) elongated parallel to the trace of the foliation and, in most cases, rimmed by plagioclase and olivine aggregates (Fig. 2c). Mylonite subdomains are fine-grained assemblages that occur either in the pressure shadow of spinel porphyroclasts or as aggregates surrounded by ultrafine-grained, anastomosing ultramylonite bands (Fig. 2c) composed of submicroscopic grains of the same minerals (compare Fig. 3h mylonite with Fig. 3g and i ultramylonite). Apart from the contact with the protomylonite zone, where mylonite subdomains are rich in olivine or plagioclase (Figs 2f and 3e) and enclosed in clinopyroxene-rich ultramylonite bands (Fig. 3f), olivine, pyroxenes, plagioclase and spinel are homogeneously distributed phases in the mineral matrix of the mylonite zone (Fig. 3g–i). As in the protomylonite, amphibole is always closely associated with plagioclase or clinopyroxene (Figs 2e and 3g–i), in contrast to plagioclase that appears disaggregated from spinel both in the mylonite and ultramylonite subdomains (Fig. 3g–i). Except for the porphyroclasts, constituent minerals throughout the mylonite zone display a unimodal grain-size distribution (Fig. 4b) and equidimensional or slightly elongated crystal shapes with straight grain boundaries (Fig. 3f–i). If elongated, olivine and clinopyroxene neoblasts show aspect ratios ranging from 1·5 to 3·0 with the longest axis parallel to the trace of the foliation plane (Fig. 3f–i).

CRYSTALLOGRAPHIC PREFERRED ORIENTATIONS

Clinopyroxene and olivine

The strength of the CPO can be quantified by the J-index—the volume-averaged integral of the squared orientation densities (Bunge, 1982)—which is sensitive to peaks in the orientation distribution function. The J-index ranges from unity for a random fabric to infinity for a single crystal; most natural peridotites show olivine J-index values between two and 20, and an average around eight (Ben Ismail & Mainprice, 1998; Tommasi *et al.*, 2000). There is a clear decrease in the intensity of the crystal preferred orientation (CPO) of both olivine and orthopyroxene from the dunite and spinel-websterite zones towards the mylonite (Fig. 4c). The olivine CPO strength is moderate in the dunite and in the Spl websterite zones (J-index 3·6–5·4); it decreases gradually towards the mylonitic shear zone, being very weak in the protomylonite (J-index 1·4–2·3) and near random in the mylonite (J-index 1·1–1·3) (Fig. 4c). Clinopyroxene CPO strength displays a similar variation; its J-index decreases from the dunite zone (4·2–4·7) through the granular pyroxenite zones (2·0–3·2) to the mylonite zone, which has very low J-indices (1·2–1·4) characteristic of a near random fabric (Fig. 4c).

In all lithologies, a weak correlation exists between clinopyroxene [001]- and olivine [100] axes, which are always distributed within the plane of the dominant foliation of the zone analyzed; that is, the high-temperature tectonite foliation in the dunite, the Spl websterite and the protomylonite zones (continuous lines in Fig. 5a and dotted lines in Fig. 5b–d, respectively), and the mylonitic foliation in the mylonite zone (horizontal lines in Fig. 5e and f). Moreover, these axes usually have maxima, which have a roughly constant orientation in all zones, being subparallel to the lineation marked by the elongation of pyroxene porphyroclasts of the mylonite zone. Except in the dunite, clinopyroxene (010) planes are subparallel to the (010) planes of olivine (Fig. 5) and both tend to be at a high angle to the dominant foliation, but this relation is locally disturbed at the contact between the protomylonites and mylonites.

The transition from the dunite and the Spl websterite towards the protomylonite and mylonites is also characterized by a change in the symmetry of olivine CPO. The dunites and Spl websterites are characterized by a clear maximum of [010] normal to the high-temperature tectonite foliation of nearby peridotites (continuous lines in Fig. 5a) and a girdle distribution of [100] in this plane (Fig. 5a). This olivine CPO pattern is similar to the one most commonly observed in peridotites of the overlying spinel tectonite domain of the Ronda Massif (Vauchez & Garrido, 2001; Soustelle *et al.*, 2009). In contrast, the protomylonites and mylonites close to the contact have a weaker CPO, but with more orthorhombic patterns.

The symmetry of the clinopyroxene and olivine CPOs can be further investigated through analysis of eigenvalues of the orientation function for each axis in terms of the relative proportion of random (R), girdle (G) and point

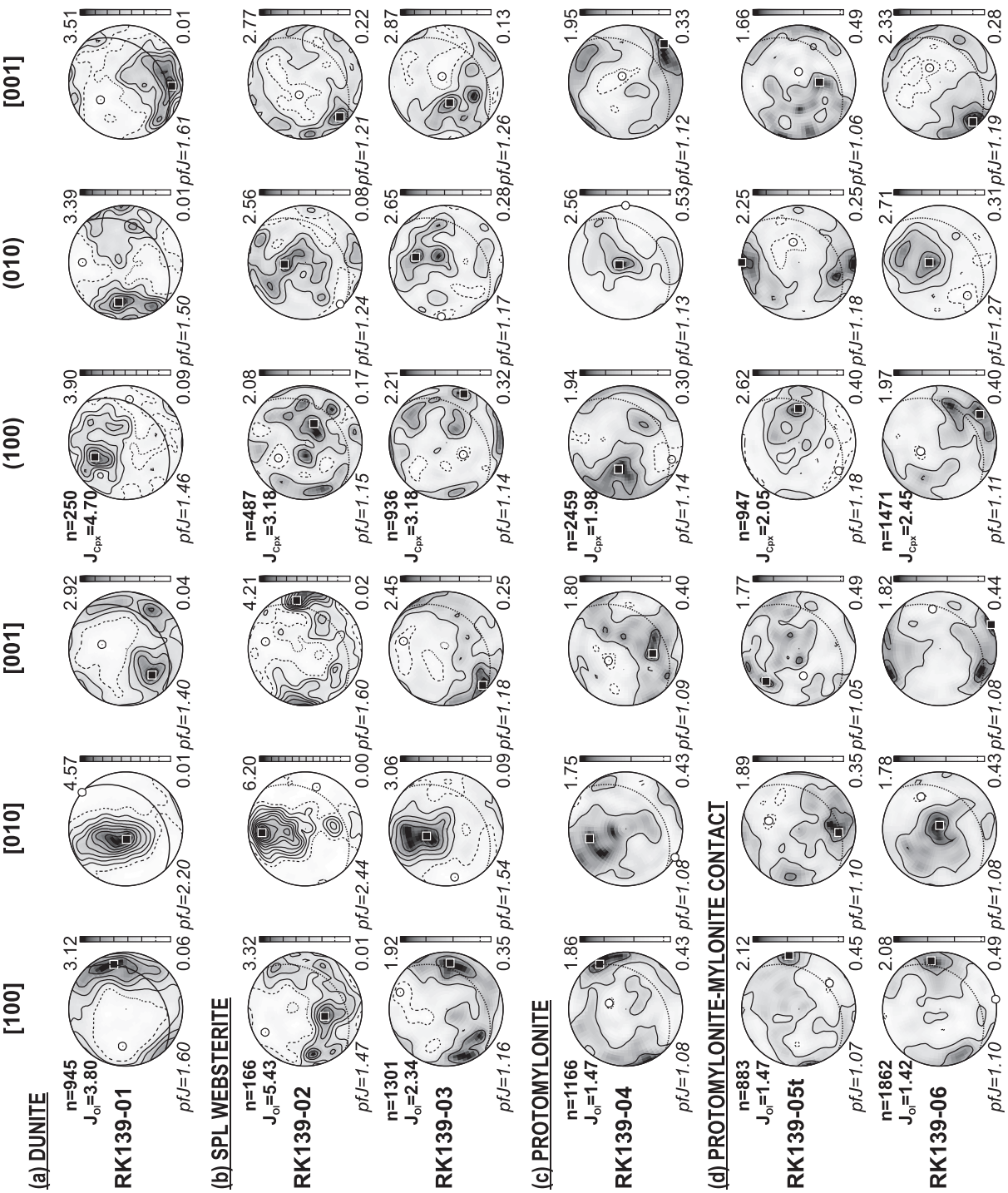

Fig. 5. (Continued)

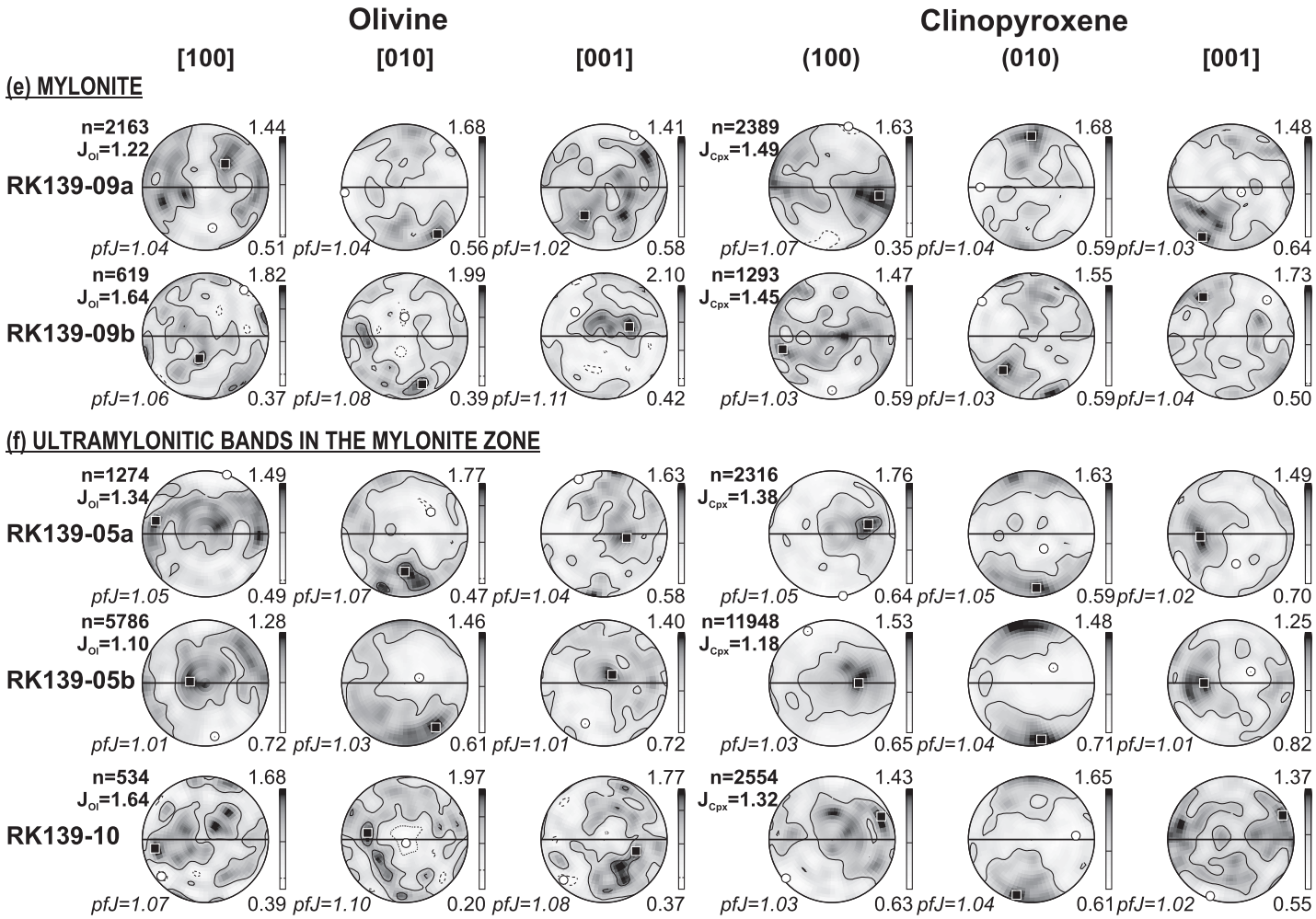

Fig. 5. (a–f) Olivine and clinopyroxene crystallographic preferred orientations (CPOs) from the dunite (a) to the ultramylonite bands of the mylonite zone (f). Lower hemisphere, equal-area stereographic projections; contours at one multiple of uniform distribution. Pole figures are plotted using average Euler angles for each grain ('one point per grain') to avoid overrepresentation of larger grains in the thin sections. All data are presented in a reference framework of the mylonite, cut perpendicular to the foliation and parallel to the lineation of the mylonite shear zone (see Fig. 3 for sample locations). Continuous lines in (a) and dotted lines in (b)–(d) indicate the trace of the high-temperature foliation of the host peridotite. Horizontal black line in (e) and (f) shows the trace of the shear zone foliation, and lineation is at the east–west poles. *n*, number of measured grains; J_{Ol} and J_{Cpx} are the J-indices (after Bunge, 1982) of olivine and orthopyroxene, respectively; pfJ is a scalar measure of the strength of the axis orientation.

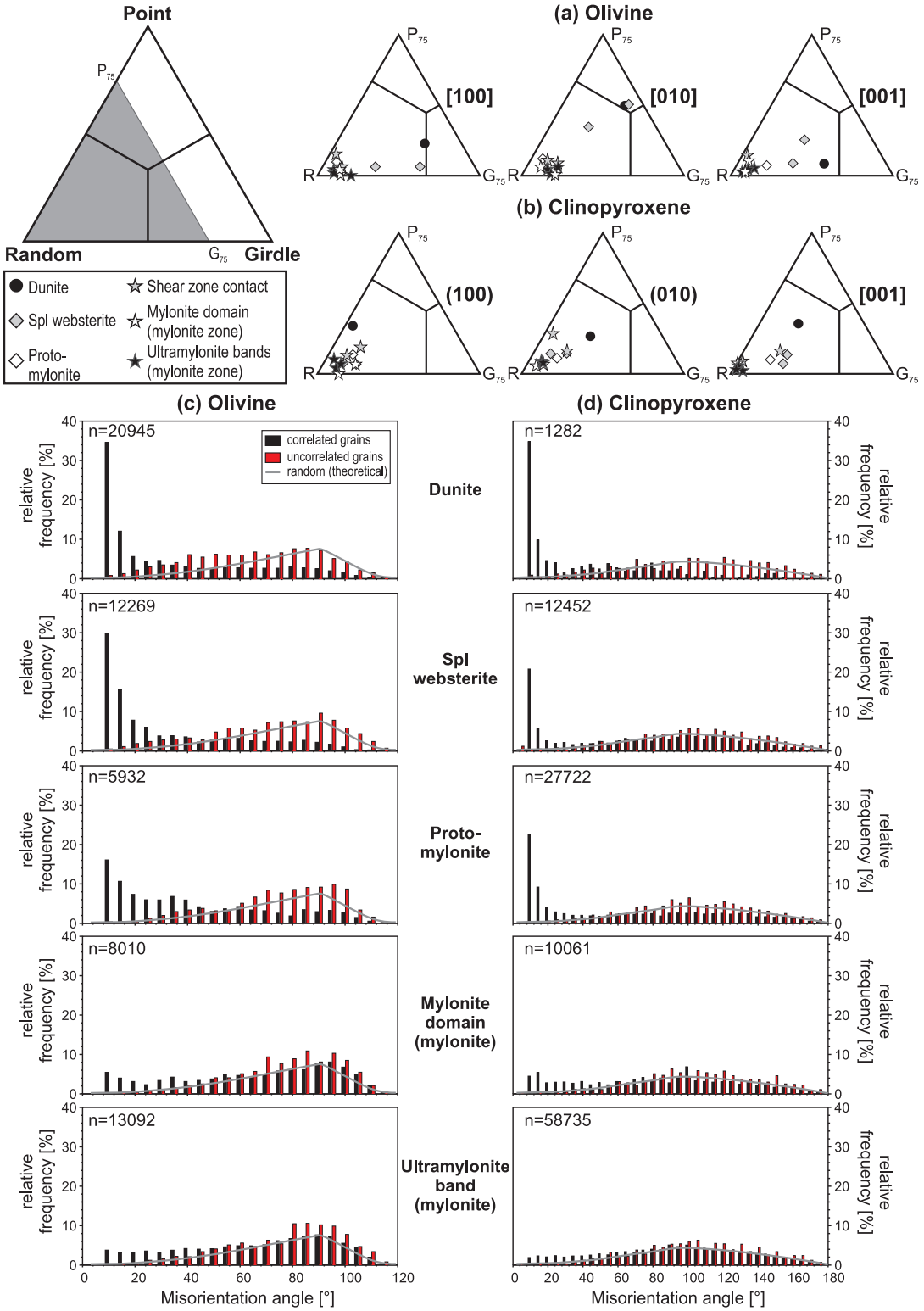

Fig. 6. Olivine (a) and clinopyroxene (b) CPO symmetry expressed as the proportion of point (P), random (R) and girdle (G) components calculated from the eigenvalues (λ_1, λ_2, λ_3) of the normalized orientation matrix for the three crystallographic axes or planes. $P = \lambda_1 - \lambda_3$, $G = 2(\lambda_2 - \lambda_3)$, $R = 3\lambda_3$ if $P + G + R = 1$. (c, d) Misorientation angle distribution for olivine (c) and clinopyroxene (d) in the various microstructural zones. Correlated misorientations (black) are measured between neighboring grains, uncorrelated misorientations (red) are measured between randomly selected points, and random indicates the theoretical distribution for a random CPO.

(P) components (Vollmer, 1990). The results of this analysis indicate that the distribution of olivine [100] and [001] axes in the dunite and Spl-websterite zones has a significant girdle component, whereas [010] axes tend to cluster around a point (Fig. 6a). Clinopyroxene (100), (010) and [001] distributions in the dunite have the highest point values (Fig. 6b), whereas significant weakening of CPO from the host peridotite towards the mylonitic shear zone is expressed by the increasing random component in the distribution of all three axes for both clinopyroxene (Fig. 6b) and olivine (Fig. 6a). This observation is also supported by increasing convergence of correlated (nearest neighbor) misorientation angle frequency histograms for olivine and clinopyroxene with that of the expected random distribution curve for the corresponding crystal symmetry class (Randle, 1993; Lloyd *et al.*, 1997; Wheeler *et al.*, 2001; Lloyd, 2004) (Fig. 6c and d). In addition, correlated misorientation histograms (measured between neighboring grains) show a clear predominance of low-angle (<15°) rotations in the dunite, Spl websterite, and in the protomylonite zones, suggesting activation of dynamic recrystallization by subgrain rotation during dislocation creep (see Amelinckx & Dekeyser, 1959; Poirier & Nicolas, 1975).

Other mineral phases

Orthopyroxene is rare; it displays a weak CPO in the Spl websterite zone, with [001] axes roughly parallel to clinopyroxene [001] axes, and shows a random fabric in the mylonitic zone. Plagioclase occurs in only the protomylonite and mylonite zones, where it has a random CPO pattern. The low abundance of spinel and amphibole (Table 1) prevents statistical analysis of their CPO and we cannot draw conclusions on their deformation mechanisms from these data.

WHOLE-ROCK AND MINERAL CHEMISTRY

Whole-rock chemistry

The whole-rock major element composition of the Spl websterite, the protomylonite and the mylonite was measured by X-ray fluorescence (XRF) using the analytical facilities of the IACT (Table 1). The composition of all zones is in the range of other websterites from this domain of the Ronda Peridotite (Garrido & Bodinier, 1999; Bodinier *et al.*, 2008). All zones show a similar Mg# in the range 0·886–0·895 and a fairly stable Na_2O content of 0·15–0·23 wt %. The Spl websterite has slightly lower Al_2O_3 (9·89 wt %) and CaO (11·7 wt %), and higher MgO (25·2 wt %) contents than the plagioclase-bearing pyroxenite zones (protomylonite and mylonite) (Fig. 4d). The protomylonite and the mylonite have a similar composition, characterized by high Al_2O_3 (11·2–14·5 wt %) and CaO (13·6–15·5 wt %), and low MgO (19·8–22·7 wt %) contents (Fig. 4d).

Mineral chemistry

Mineral major element compositions (Fig. 7; Table 2; Supplementary Data Table A1, available for downloading at http://www.petrology.oxfordjournals.org) were determined using CAMECA SX-100 and SX-50 electron microprobes at the Scientific Instrumentation Center of the University of Granada (CIC-UGR, Granada) and at the Scientific and Technological Centers of the University of Barcelona, respectively. Analyses were carried out using accelerating voltages of 20–15 kV, a sample current of 15 nA (except for Na, where 5 nA was applied), a beam diameter of 5 μm and counting times of 10–20 s. Natural and synthetic silicate and oxide standards were used for calibration and a ZAF correction was applied. Because of their very small grain size, only a few valid analyses of minerals were obtained in the mylonite zone.

Major element mapping of spinel (Fig. 8) and textural and qualitative analyses of amphibole (Fig. 2d and e) were obtained using a Leo 1430VP and a FEI Quanta 400 SEM (CIC-UGR, Granada) equipped with energy-dispersive spectroscopic (EDS) detectors. EDS analyses were carried out using accelerating voltages of 20 kV and a sample beam current of 1 nA.

Olivine

Olivine has forsterite-rich (Fo) composition in all zones. It has a roughly constant Fo content of 0·90 in the dunite and Spl websterite that decreases (0·875–0·883) towards the mylonitic shear zone (Table 2).

Pyroxenes

Clinopyroxene in all zones shows core to rim zoning characterized by decreasing Al, Na and Cr contents (Table 2; Fig. 7a and c). Ca and Mg# show overall flat profiles with only minor enrichment towards the rims (Fig. 7a and c). The CaO (22·9–24·1 wt %) and Na_2O (0·1–0·3 wt %) contents of clinopyroxene cores, as well as their Mg# (0·901–0·930), are similar in all zones, in contrast to the Al_2O_3 concentrations, which are higher in the dunite and spinel websterite (usually 3·5–7·2 wt %) than in the mylonite (usually 1·7–2·2 wt % within the shear zone) (Table 2).

From dunite to mylonite, orthopyroxene cores show increasing Al_2O_3 (from 3·9 to 6·2 wt %) and slightly decreasing Cr_2O_3 contents (from 0·5 to 0·2 wt %) with overlapping CaO concentrations (0·5–0·7 wt %) and Mg# (0·89–0·90) (Table 2). Mineral rims are consistently more depleted in Al and Ca than the corresponding cores (Fig. 7b and d). The major element compositions of clino- and orthopyroxene in the profiles presented in Fig. 7 are given in the Supplementary Data (Table A1).

Table 1: Whole-rock major element composition of the studied samples (in wt %) and average modal compositions of the microstructural domains†*

	Coarse-grained pyroxenite		Fine-grained pyroxenite shear zone
Zone	Spl websterite	Protomylonite	Mylonite
Ol	11·5	12·9	13·5
Opx	9·6	5·7	5·4
Cpx	65·5	66·3	57·4
Spl	13·4	5·7	5·5
Plag	0·0	8·8	16·7
Amp	0·0	0·5	1·5

Sample:	RK139-02	RK139-03/04	RK139-05T	RK139-05B	RK139-07/10	RK139-11
SiO_2	44·2	44·7	45·8	44·7	45·4	44·5
TiO_2	0·15	0·17	0·14	0·15	0·15	0·15
Al_2O_3	9·89	11·3	11·2	11·6	13·0	14·5
Cr_2O_3	0·46	0·42	0·35	0·38	0·30	0·30
FeO_t	5·26	4·86	4·67	5·09	4·57	4·56
MnO	0·12	0·12	0·12	0·12	0·12	0·12
MgO	25·2	22·7	21·2	22·9	20·3	19·8
NiO	0·13	0·12	0·09	0·10	0·08	0·08
CaO	11·7	13·6	15·4	14·3	15·5	14·9
Na_2O	0·23	0·22	0·18	0·15	0·15	0·20
K_2O	0·01	0·01	0·01	0·01	0·01	0·02
P_2O_5	b.d.l.	0·01	0·01	0·01	0·01	b.d.l.
LOI	2·80	1·85	0·79	0·33	0·32	0·76
Total	100·1	100·0	99·9	99·9	99·9	99·9
mg#	0·8950	0·8929	0·8901	0·8892	0·8877	0·8855

*Samples were crushed and pulverized in a Pulverisette agate mortar. X-ray fluorescence (XRF) analysis of major and minor transition elements (e.g. Ni, Cr) in whole-rocks was carried out at the Center of Scientific Instruments of the University of Granada (CIC-UGR, Granada, Spain).
†Mineral modes were reconstructed by averaging the mass-balance of whole-rock and mineral major element compositions, using the total inversion method of Tarantola & Valette (1982). Modal proportions are presented in weight per cent. b.d.l., below detection limit; FeO_t, all iron reported as Fe^{2+}; LOI, loss on ignition; mg# = [Mg/(Mg + Fe)] in cation ratio. Amp, amphibole; Cpx, clinopyroxene; Ol, olivine; Opx, orthopyroxene; Plag, plagioclase; Spl, spinel.

Spinel and plagioclase

In general, spinel in the dunite and in the Spl websterite is poorer in Al_2O_3 (50·8–57·3 wt %) and richer in Cr_2O_3 (14·5–16·5 wt %) than in the plagioclase-bearing microstructural zones (59·6–62·6 wt % and 2·8–6·5 wt %, respectively), but is characterized by a relatively constant MgO and FeO content as denoted by the overlapping Mg# range of 0·73–0·78 irrespective of lithology (Table 2). However, internal zoning of spinel is more complex than that of the other mineral phases. The long axes of elongated spinel grains, which lie parallel to the lineation, show a maximum concentration of Al and a minimum of Cr at their tips, in contrast to the short-axis rims, which show a minimum concentration of Al and a maximum of Cr (Fig. 8). This multipolar Al–Cr zoning is a well-known phenomenon in orogenic and ophiolitic peridotites, where it is attributed to stress-induced diffusion creep (combination of Nabarro–Herring creep and Coble creep) (Ozawa, 1989).

Plagioclase in protomylonite and mylonite has overlapping anorthite-rich compositions, with mylonite plagioclase having slightly higher anorthite contents than that in protomylonite (An 0·97–0·98 vs 0·94–0·97, respectively) (Table 2). Plagioclase rims have similar composition to

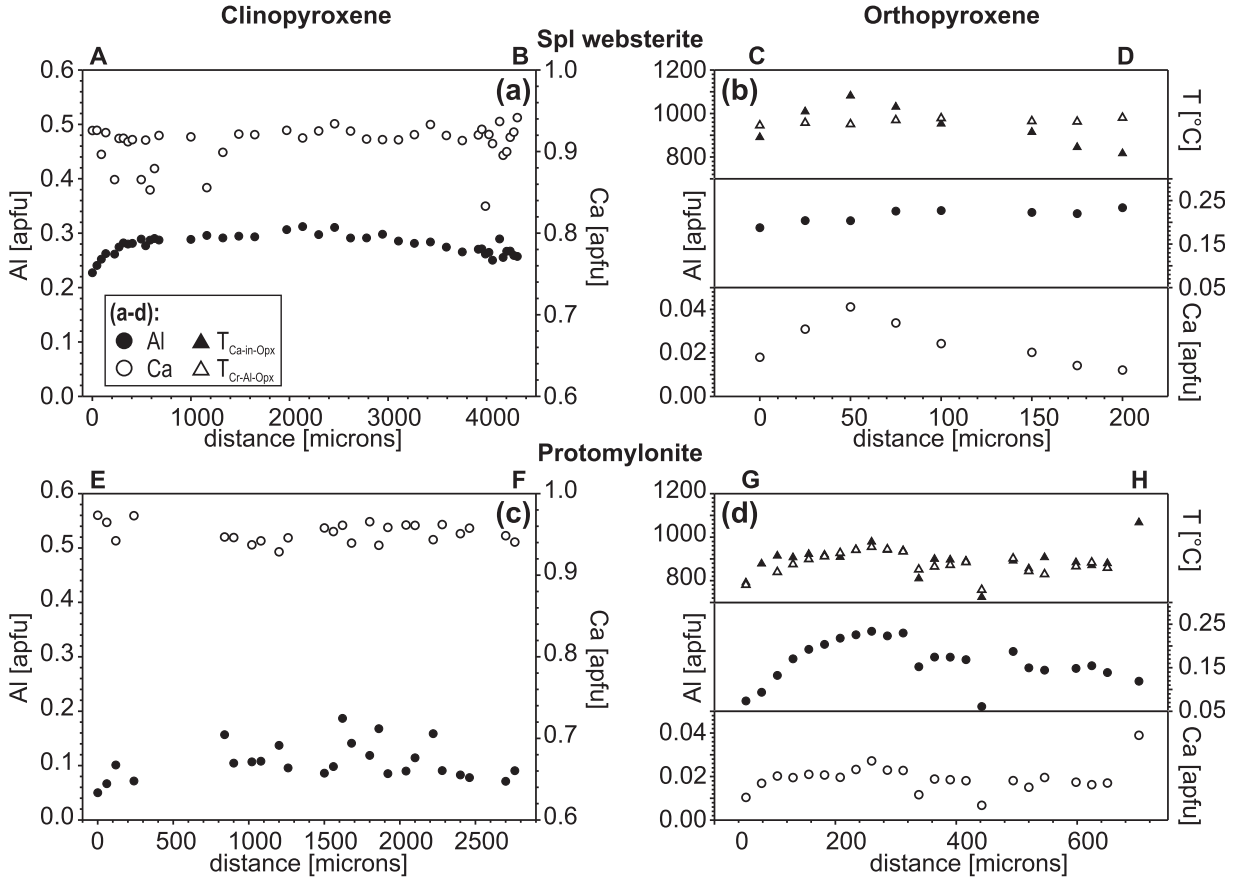

Fig. 7. Major element chemical composition across clinopyroxene and orthopyroxene porphyroclasts from the Spl websterite (a, b) and protomylonite zones (c, d). Temperature was calculated using the Ca-in-Opx method ($T_{Ca\text{-}in\text{-}Opx}$) of Brey & Köhler (1990) and the Cr–Al-Opx method ($T_{Cr\text{–}Al\text{-}Opx}$) of Witt-Eickschen & Seck (1991). [For locating the profiles refer to Fig. 2b for Spl websterite (A–B and C–D) and Fig. 2c for the protomylonite (E–F and G–H).] apfu, atom per formula unit calculated for six oxygens from the wt % major element data (Supplementary Data Table A1).

cores; where in contact with spinel, the An content of plagioclase in contact with the long axis of spinel (An 0·961–0·970) is slightly higher than for plagioclase in contact with spinel short axis tips (An 0·955–0·968).

Amphibole

Because of its small grain size, only one valid electron microprobe analysis of amphibole is available from the mylonite zone. This measurement shows that it is a calcic amphibole (Table 2). This was also confirmed by qualitative SEM–EDS spectra.

CONSTRAINTS ON DEFORMATION CONDITIONS

Pressure and temperature

Conventional geothermometry

Geothermometric formulations for spinel–plagioclase websterites are essentially the same as those applied to spinel peridotites (Nimis & Grütter, 2010). We estimate temperatures using the Ca content in orthopyroxene (Ca-in-Opx) formulation of Brey & Köhler (1990), and the Al in orthopyroxene (Al-in-Opx) formulation of Witt-Eickschen & Seck (1991). Although this latter formulation was designed for spinel peridotites, it is applicable to all our samples because the exchange of Cr and Al is controlled by spinel and pyroxene, which are present in all zones, and the Cr content of orthopyroxene falls within the range of applicability of this formulation (Witt-Eickschen & Seck, 1991).

Calculated equilibrium temperatures using orthopyroxene core compositions yield similar temperatures irrespective of the geothermometer used and lithology (at 1·0 GPa, 920–980°C for Ca-in-Opx, and 955–1005°C for the Al-in-Opx) (Fig. 7b and d). Temperatures calculated using core composition are minimum values for peak temperatures because exsolution of secondary pyroxene and spinel in pyroxenes (Obata, 1980; Lenoir *et al.*, 2001) is not integrated here. Temperatures using orthopyroxene rim compositions range from 860 to 890°C (at 1·0 GPa) for both formulations

Table 2: Representative electron microprobe analyses of minerals

Dunite:	Cpx						Spl						Opx				Ol			
	core			rim			core			rim			core		rim		core		rim	
SiO_2	52·1	51·3	52·5	52·9	52·9	52·3	0·03	0·03	0·02	0·04	0·01	0·00	53·4	54·5	56·2	55·7	40·2	39·6	39·8	39·8
TiO_2	0·13	0·13	0·16	0·17	0·12	0·15	0·08	0·06	0·03	0·06	0·06	0·02	0·03	0·02	0·03	0·01	0·00	0·00	0·04	0·03
Al_2O_3	4·19	5·38	3·50	3·28	2·70	3·20	50·9	50·8	52·0	52·1	52·7	53·2	3·87	4·84	2·41	3·38	0·03	0·00	0·01	0·00
Cr_2O_3	0·70	0·89	0·70	0·73	0·54	0·76	16·5	16·4	15·9	15·2	13·8	13·5	0·54	0·57	0·27	0·24	0·02	0·05	0·02	0·02
FeO	2·24	2·45	2·32	2·31	2·01	2·29	12·1	12·1	11·9	11·7	12·5	12·0	6·44	6·21	6·55	6·65	9·65	9·72	9·99	9·75
MnO	0·10	0·10	0·08	0·13	0·09	0·06	0·14	0·13	0·13	0·12	0·11	0·12	0·10	0·14	0·13	0·14	0·17	0·18	0·13	0·17
NiO	0·00	0·04	0·05	0·00	0·01	0·04	0·31	0·26	0·29	0·32	0·29	0·27	0·00	0·08	0·06	0·09	0·33	0·40	0·35	0·38
MgO	16·9	15·7	16·6	16·9	16·7	16·8	18·8	18·6	18·8	19·3	19·3	18·9	33·8	31·5	32·8	33·1	49·8	49·1	49·7	49·9
CaO	23·3	22·4	23·0	23·8	23·5	23·1	0·00	0·00	0·00	0·00	0·00	0·00	0·59	1·64	0·49	0·44	0·03	0·03	0·01	0·04
Na_2O	0·30	0·30	0·27	0·23	0·22	0·30	0·00	0·00	0·00	0·00	0·00	0·00	0·02	0·03	0·02	0·01	0·00	0·00	0·00	0·00
K_2O	0·00	0·02	0·01	0·00	0·02	0·02	0·00	0·00	0·00	0·00	0·00	0·00	0·00	0·02	0·03	0·01	0·00	0·00	0·00	0·00
Total	99·9	98·7	99·2	100·4	98·7	99·1	98·9	98·3	99·2	98·9	98·8	98·0	98·7	99·5	98·9	99·8	100·2	99·1	100·1	100·1
mg#	0·931	0·919	0·927	0·929	0·937	0·929	0·736	0·734	0·738	0·747	0·734	0·737	0·903	0·900	0·899	0·899	0·902	0·900	0·899	0·901
cr#							0·178	0·178	0·170	0·163	0·149	0·145								

Spl webst.:	Cpx						Spl						Opx				Ol			
	core			rim			core	long-rim	short-rim	core	long-rim	short-rim	core		rim		core		rim	
SiO_2	50·8	50·5	50·3	51·2	51·9	51·4	0·00	0·03	0·05	0·04	0·04	0·78	54·2	53·4	54·1	54·4	40·5	39·1	40·7	39·8
TiO_2	0·13	0·12	0·10	0·13	0·17	0·16	0·01	0·02	0·00	0·03	0·00	0·03	0·00	0·02	0·03	0·05	0·01	0·02	0·00	0·00
Al_2O_3	6·76	5·71	6·94	5·81	4·62	5·14	61·2	62·6	60·7	61·5	59·6	58·5	5·49	5·72	4·29	4·35	0·00	0·01	0·00	0·04
Cr_2O_3	0·45	0·68	0·34	0·34	0·54	0·43	6·33	4·72	6·77	4·60	6·24	7·74	0·28	0·21	0·29	0·25	0·02	0·02	0·00	0·08
FeO	2·64	2·21	2·75	2·43	2·45	2·37	10·4	9·79	10·1	10·8	10·9	11·1	6·71	6·83	6·98	7·14	9·70	9·53	10·1	9·85
MnO	0·12	0·14	0·12	0·14	0·16	0·12	0·10	0·11	0·02	0·16	0·08	0·14	0·12	0·21	0·16	0·24	0·10	0·13	0·20	0·11
NiO	0·00	0·00	0·00	0·00	0·00	0·04	0·42	0·42	0·41	0·36	0·40	0·35	0·00	0·00	0·00	0·00	0·44	0·37	0·39	0·45
MgO	15·9	16·2	15·7	16·1	16·9	16·0	21·7	21·7	21·1	21·1	21·0	19·9	33·3	32·8	33·7	33·5	50·4	50·5	50·5	50·0
CaO	23·4	23·9	23·4	23·7	23·9	23·6	0·00	0·00	0·00	0·00	0·00	0·00	0·68	0·66	0·48	0·49	0·00	0·02	0·00	0·01
Na_2O	0·26	0·29	0·22	0·30	0·21	0·21	0·00	0·00	0·00	0·00	0·00	0·00	0·06	0·00	0·00	0·04	0·00	0·00	0·00	0·00
K_2O	0·00	0·00	0·00	0·00	0·00	0·01	0·00	0·00	0·00	0·00	0·00	0·00	0·00	0·00	0·00	0·01	0·00	0·00	0·00	0·00
Total	100·5	99·7	99·9	100·2	100·8	99·5	100·1	99·4	99·1	98·5	98·3	98·5	100·9	99·8	100·0	100·5	101·2	99·7	101·9	100·4
mg#	0·915	0·929	0·911	0·922	0·925	0·923	0·789	0·798	0·789	0·776	0·775	0·762	0·898	0·895	0·896	0·893	0·903	0·904	0·900	0·901
cr#							0·065	0·048	0·070	0·048	0·066	0·082								

Proto-myl.:	Cpx						Spl						Plag			
	core			rim			core	long-rim	short-rim	core	long-rim	short-rim	core		rim	
SiO_2	50·0	49·9	50·9	52·4	52·2	52·0	0·00	0·01	0·03	0·02	0·83	0·05	43·7	42·7	42·9	42·1
TiO_2	0·10	0·11	0·11	0·10	0·17	0·11	0·07	0·01	0·03	0·04	0·03	0·00	0·00	0·00	0·01	0·00
Al_2O_3	5·80	5·85	6·66	2·50	2·68	2·86	59·6	60·1	57·6	61·3	61·6	57·6	35·6	34·8	34·9	34·7
Cr_2O_3	0·31	0·26	0·35	0·26	0·37	0·21	6·51	6·49	8·58	5·17	3·77	8·38	0·00	0·00	0·00	0·00
FeO	2·88	2·90	2·83	2·65	2·50	2·71	12·4	11·4	12·6	12·4	11·9	13·2	0·09	0·00	0·12	0·20
MnO	0·13	0·13	0·10	0·08	0·09	0·08	0·15	0·09	0·20	0·12	0·13	0·14	0·00	0·00	0·00	0·00
NiO	0·00	0·02	0·04	0·00	0·00	0·00	0·35	0·37	0·37	0·35	0·34	0·27	0·00	0·00	0·00	0·00
MgO	15·7	15·2	15·4	17·2	17·1	17·0	19·4	20·3	19·3	20·0	19·5	18·6	0·01	0·03	0·00	0·00
CaO	23·8	23·3	23·1	23·9	23·9	23·9	0·00	0·00	0·00	0·00	0·00	0·00	19·6	19·5	19·5	19·7
Na_2O	0·15	0·20	0·25	0·14	0·19	0·14	0·00	0·00	0·00	0·00	0·00	0·00	0·40	0·38	0·41	0·44
K_2O	0·00	0·02	0·02	0·01	0·00	0·00	0·00	0·00	0·00	0·00	0·00	0·00	0·01	0·02	0·00	0·01
Total	98·9	97·9	99·8	99·3	99·2	99·1	98·6	98·7	98·7	99·3	98·1	98·2	99·4	97·4	97·7	97·2
mg#	0·907	0·904	0·906	0·921	0·925	0·918	0·736	0·761	0·733	0·742	0·746	0·716				
cr#							0·068	0·068	0·091	0·054	0·039	0·089				
An													0·964	0·966	0·963	0·961

(continued)

Table 2: Continued

Proto-myl.:	Opx						Ol					
	core			rim			core			rim		
SiO_2	53·0	53·7	53·2	55·0	54·5	54·2	40·2	40·2	39·8	40·2	39·6	41·0
TiO_2	0·03	0·05	0·03	0·04	0·01	0·00	0·03	0·02	0·00	0·00	0·00	0·00
Al_2O_3	6·18	5·49	5·57	3·61	2·82	2·77	0·00	0·01	0·00	0·00	0·00	0·00
Cr_2O_3	0·19	0·19	0·14	0·14	0·20	0·22	0·03	0·03	0·04	0·00	0·00	0·00
FeO	7·32	7·71	7·10	7·17	7·59	7·27	11·2	11·8	12·2	11·5	11·7	11·0
MnO	0·13	0·19	0·20	0·20	0·20	0·23	0·23	0·22	0·24	0·25	0·25	0·23
NiO	0·00	0·00	0·09	0·00	0·06	0·06	0·37	0·26	0·33	0·25	0·31	0·29
MgO	32·6	32·7	31·4	33·7	32·3	32·2	48·4	48·1	48·5	48·7	47·9	48·0
CaO	0·55	0·54	0·59	0·42	0·47	0·52	0·02	0·05	0·01	0·01	0·04	0·03
Na_2O	0·00	0·04	0·00	0·04	0·00	0·00	0·00	0·00	0·00	0·00	0·00	0·01
K_2O	0·00	0·00	0·02	0·00	0·01	0·01	0·00	0·00	0·00	0·00	0·00	0·02
Total	100·0	100·7	98·4	100·3	98·1	97·5	100·5	100·6	101·1	100·9	99·9	100·5
mg#	0·888	0·883	0·888	0·893	0·883	0·888	0·885	0·879	0·876	0·883	0·879	0·886

Myl.:	Cpx				Spl				Plag				Ultra-myl:	Cpx		Spl	Plag		Amp
	core		rim		core		rim		core		rim								
SiO_2	53·2	54·1	54·1	53·8	0·02	0·02	0·03	0·04	43·7	43·5	43·4	43·3	SiO_2	53·2	53·2	0·04	43·1	42·9	42·9
TiO_2	0·12	0·09	0·06	0·12	0·01	0·03	0·03	0·04	0·02	0·00	0·00	0·01	TiO_2	0·12	0·12	0·02	0·00	0·01	0·05
Al_2O_3	2·11	1·73	1·76	2·29	64·0	64·0	63·1	63·7	35·9	35·8	35·7	36·2	Al_2O_3	2·10	1·94	52·7	36·0	35·9	12·1
Cr_2O_3	0·28	0·26	0·22	0·19	2·74	2·74	3·82	3·00	0·00	0·03	0·01	0·02	Cr_2O_3	0·14	0·24	14·1	0·00	0·01	0·44
FeO	2·81	2·81	2·73	2·56	12·9	12·8	12·8	12·5	0·14	0·16	0·14	0·09	FeO	2·55	2·48	15·5	0·23	0·14	5·82
MnO	0·15	0·14	0·11	0·15	0·14	0·18	0·15	0·10	0·01	0·00	0·00	0·02	MnO	0·08	0·10	0·22	0·00	0·00	0·17
NiO	0·02	0·02	0·04	0·04	0·33	0·35	0·36	0·38	0·03	0·01	0·00	0·00	NiO	0·06	0·06	0·22	0·01	0·02	0·09
MgO	17·1	17·1	17·1	16·9	20·1	19·9	20·0	20·2	0·01	0·01	0·02	0·02	MgO	17·7	17·1	17·0	0·03	0·02	23·3
CaO	24·0	23·6	23·8	23·9	0·00	0·00	0·00	0·00	19·7	19·7	19·8	19·8	CaO	23·8	24·4	0·15	20·1	19·9	14·8
Na_2O	0·15	0·17	0·16	0·18	0·00	0·00	0·00	0·00	0·27	0·21	0·23	0·24	Na_2O	0·24	0·14	0·00	0·23	0·22	0·06
K_2O	0·02	0·02	0·02	0·02	0·03	0·00	0·00	0·00	0·02	0·03	0·02	0·01	K_2O	0·03	0·01	0·01	0·02	0·02	0·01
Total	100·0	100·1	100·0	100·1	100·2	100·1	100·3	100·0	99·8	99·5	99·4	99·7	Total	99·9	99·7	99·9	99·6	99·1	99·7
mg#	0·916	0·916	0·918	0·922	0·734	0·735	0·737	0·742					mg#	0·925	0·925	0·661			0·877
cr#					0·028	0·028	0·039	0·031					cr#			0·153			
An									0·976	0·981	0·979	0·978	An				0·980	0·980	

Amp, amphibole; Cpx, clinopyroxene; Ol, olivine; Opx, orthopyroxene; Plag, plagioclase; Spl, spinel. An = Ca/(Ca + Na); cr# = Cr/(Cr + Al); mg# = Mg/(Mg + Fe).

(Fig. 7b and d). The two-pyroxene thermometer formulations of Taylor (1998) and Brey & Köhler (1990) applied to clinopyroxene–orthopyroxene pairs in textural contact show the same decreasing temperature trend between cores and rims, but yield relatively lower temperatures than single orthopyroxene thermometers: 905–920°C for the cores and 740–750°C for the rims (at 1·0 GPa).

Textural and phase equilibrium constraints on P–T *conditions of deformation*

The occurrence of plagioclase as a metamorphic rim around spinel (Fig. 3d and e) indicates that cooling (Fig. 7b and d) was associated with decompression and that the studied pyroxenite preserves evidence of the phase transition reaction from spinel to plagioclase facies according to the reaction En + Di + Spl = An + 2Fo (CMAS system), where An is anorthite, Di is diopside, En is enstatite, Fo is forsterite and Spl is spinel. Pyroxenes and spinel are not found at olivine–plagioclase grain boundaries, showing that the reverse reaction from plagioclase to spinel facies did not occur.

The modal content of plagioclase in the protomylonite is 9%. This increases to an average of 15% within the mylonitic shear zone (locally up to 25%) (Fig. 4a). In addition, the modal content of olivine in the plagioclase-free Spl websterite is ~10%, in contrast to the plagioclase-bearing pyroxenites, where olivine contents of 12–13% were determined (locally up to 20–30%) (Fig. 4a). Similarly, the

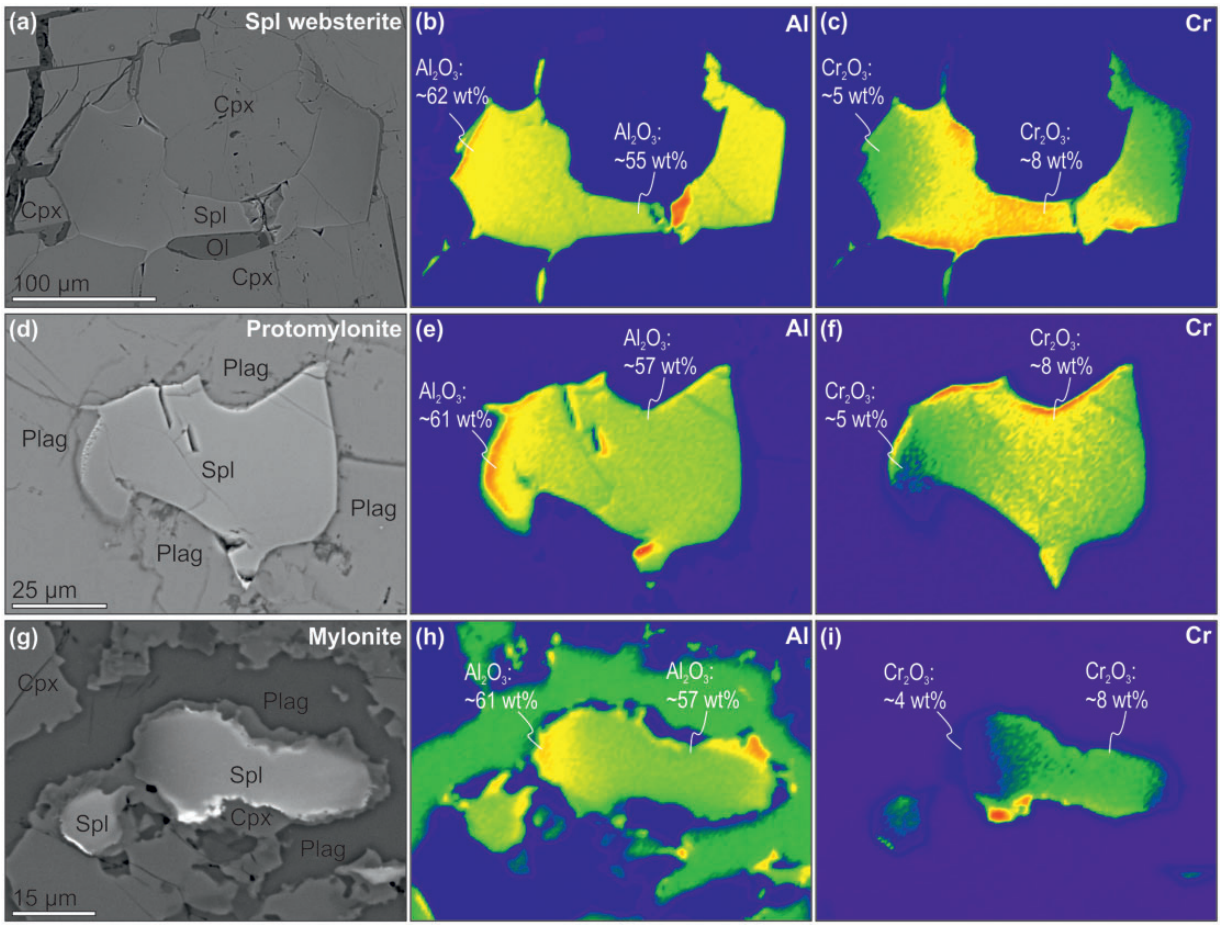

Fig. 8. Stress-induced heterogeneous distribution of Cr and Al in spinel (Ozawa, 1989) from the Spl websterite (a–c), protomylonite (d–f) and mylonite zones (g–i). Cpx, clinopyroxene; Ol, olivine; Plag, plagioclase; Spl, spinel.

modal abundance of orthopyroxene and clinopyroxene shows a decreasing trend from the plagioclase-free pyroxenite towards the mylonitic shear zone (Opx from 10% to 5%; Cpx from 65% to 57%) (Fig. 4a). Spinel core compositions are generally richer in Al in the plagioclase-bearing zones than elsewhere in the websterite or in the dunite (Table 2). The only exceptions are from the ultramylonitic bands of the mylonite zone, where spinel cores may exhibit Cr-rich compositions (Table 2). This observation is in agreement with the compositional range of spinel rims, which shows an overall increased Cr content in the rims with respect to the cores, even though the distribution of Al and Cr in the rims is heterogeneous and correlated with mineral lineation (Fig. 8). This systematic variation of modal composition and spinel chemistry within the different microstructural zones suggests a reaction between pyroxenes and spinel to produce plagioclase, olivine and Cr-rich spinel where the aluminous component in spinel is selectively consumed as the reaction proceeds (Green & Hibberson, 1970). The smaller grain size of olivine where it is found in interstitial patches around spinel–plagioclase clusters (Fig. 3d and e), and the different major element composition of these olivines in the plagioclase-bearing websterite zones with respect to those in the plagioclase-free assemblages (e.g. Mg# in Table 2) confirm the secondary origin of these minerals as a result of the phase transformation reaction.

The significance of the observed phase relations has been further evaluated using three representative subsamples from the Spl websterite, the protomylonite and the mylonite zones. Based on the restricted bulk composition variation of these subsamples (Table 1 and white stars in Fig. 9a–c) it is possible to establish with confidence the relative changes in pressure and temperature conditions from pre- to synkinematic conditions. These *P*–*T* estimates are based on core–rim compositions of the protomylonite (RK139-5T) where the system failed to fully equilibrate to the lower *P*–*T* conditions (Fig. 9b). On the other hand, equilibrium was most probably attained in the less deformed Spl websterite (Fig. 9a) and the

mylonite (Fig. 9c), which further supports these P–T estimates. Subsolidus phase relations for RK139-5T have been computed under water-saturated conditions in the NCMASH system using PerpleX (Connolly, 2009), and the updated internally consistent thermodynamic dataset of Holland & Powell (1998, updated in 2002). Theoretical considerations and simplification of the system are explained in Appendix A. Figure 9d shows the computed isochemical section for sample RK139-5T. The assemblage in the Spl websterite zone (Cpx + Opx + Ol + Spl ± Amph) is stable from *c.* 0·7 to 1·6 GPa at 1000°C in the NCMASH system. It has been well known since early experimental studies that the Al content in pyroxene is highly sensitive to changes in temperature or pressure when coexisting with spinel or plagioclase, respectively. Therefore the concomitant appearance of plagioclase and the Al depletion in pyroxene (Fig. 7) strongly support a decompression path during deformation from 0·8–1·2 GPa to 0·3–0·4 GPa based on the Al content in Opx (Fig. 9e). Because of the implications for the possible stability of amphibole during deformation in the studied samples (maximum 1·5 wt %; Table 1, Fig. 4a) all available amphibole solid solutions were tested to check the consistency of the Dale *et al.* (2005) model. This model predicts the coexistence of two amphiboles at temperatures lower than 750°C, corresponding to orthopyroxene-free assemblages (fields marked with asterisk in Fig. 9d). Comparable amphibole stability limits are obtained if pure pargasite and tremolite are considered. Therefore, cooling during decompression from 950–1000°C to 750–800°C is also constrained by the occurrence of small amounts of amphibole (*c.* 1·0–1·5 vol. %) in the low-pressure assemblage (Fig. 9f).

Water in nominally anhydrous minerals

In addition to molecular water occurring as fluid or melt inclusions, hydrogen protons can enter the structure of nominally anhydrous minerals (NAMs) (e.g. pyroxenes, olivine and plagioclase) at lattice defects forming hydroxyl groups (OH), where they can reach concentrations of several hundred ppm of equivalent H_2O. It is well known that trace amounts of structurally bound 'water' as hydroxyl groups can lower the mechanical strength of the host mineral (Mackwell *et al.*, 1985; Chen *et al.*, 1998) and thus may have a great influence on the deformation conditions. To detect molecular water and hydroxyl groups in the studied samples, double-polished thick sections (140–170 μm) were prepared from three representative samples corresponding to the Spl websterite, the protomylonite and the mylonite zones of the studied cross-section. Hydroxyl and H_2O-related absorption bands in NAMs were obtained with unpolarized light incident on randomly oriented grains using a Bruker Tensor 27 Fourier transform infrared (FTIR) spectrometer mounted on a Bruker Hyperion infrared microscope coupled with a nitrogen-cooled MCT detector at the Research School of Earth Sciences (ANU, Australia). The FTIR data are reported in Table 3. Square apertures of 80 μm × 80 μm and 40 μm × 40 μm were used for the porphyroclasts and neoblasts, respectively. In the mylonite zone the grain size was too small to perform analysis on single grains; therefore, an aperture of 100 μm × 100 μm was used on the clinopyroxene-rich matrix. A spectrum baseline was subtracted with the 'concave rubber band tool' after three iterations, using the software OPUS (Bruker, Inc.). Quantification of 'water' related to hydroxyl groups in NAMs (Table 3) was achieved following the approach of Kovács *et al.* (2008), theoretically derived by Sambridge *et al.* (2008), for weakly absorbent anisotropic minerals where the average of the unpolarized absorbance for a population of randomly oriented grains approximates to one-third of the total absorbance (i.e. sum of the absorbance along the three principal directions). Errors in the total integrated absorbance using this method are typically 10% and mainly depend on the uncertainty on the thickness and the number of grains (10–15) used for the average (Kovács *et al.*, 2008; Sambridge *et al.*, 2008) (Table 3). Integral molar absorbance coefficients for clinopyroxene (Bell *et al.*, 1995) and plagioclase (Johnson & Rossman, 2003) were used to quantify their 'water' content. Taking into account the error in thickness of the sections and in the molar extinction coefficient, the uncertainty on the absolute 'water' content is *c.* 30% in the worst case. Nevertheless, the uncertainty in relative changes is much less and usually ranges in the order of 10–15%. Owing to their low modal occurrence and small grain size in the pyroxenite it was not possible to obtain reliable spectra for olivine and orthopyroxene.

Unpolarized light infrared spectra of clinopyroxene porphyroclast cores are characterized by three major bands close to 3640, 3545 and 3465 cm^{-1} and a weak band at 3350 cm^{-1} (Fig. 10a). The position of these bands is consistent with those identified in mantle pyroxenes worldwide (Peslier *et al.*, 2002; Skogby, 2006) and they are interpreted to be related to structurally bound hydroxyl groups. Minor peaks at 3710 and 3680 cm^{-1} (marked with an asterisk in Fig. 10a) are extrinsic defects such as hydrous phases, most probably submicroscopic pargasite and/or tremolite (Della Ventura *et al.*, 2003), and were not considered during quantification as they might be related to late retrogression. In contrast to the porphyroclast cores, unpolarized light spectra of clinopyroxene neoblasts and porphyroclast rims in each microstructural zone are characterized by a broad band centered at 3550 and 3440 cm^{-1}, respectively (Fig. 10b). The band centered at 3440 cm^{-1} is typical for H_2O-rich fluid inclusions (Johnson & Rossman, 2004), whereas the one centered at higher wavenumbers is tentatively interpreted as H_2O and OH^- dissolved in minute amounts of silicate glass (see Hidas *et al.*, 2010). Nevertheless, even in the

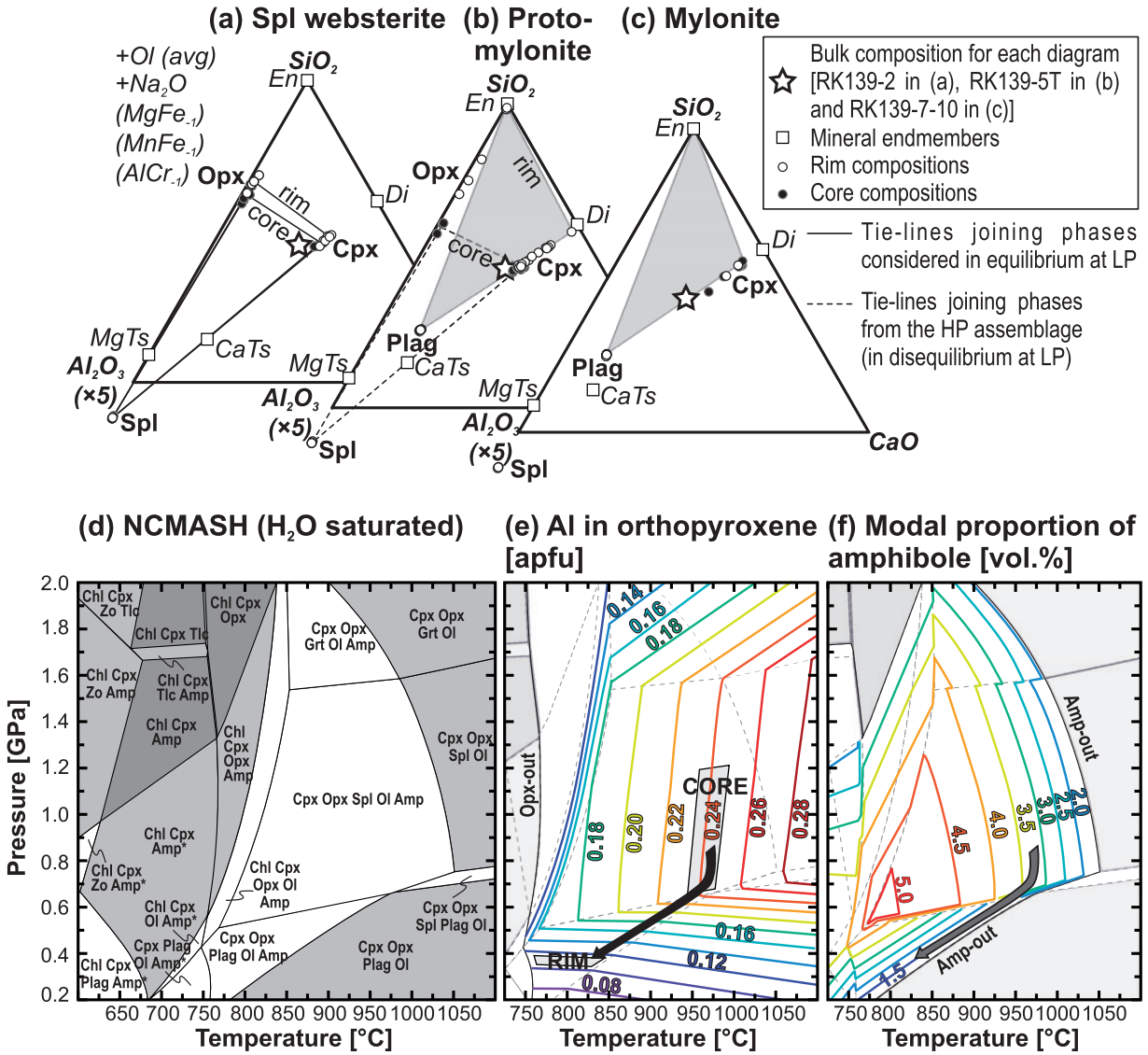

Fig. 9. Al_2O_3–CaO–SiO_2 projections showing the major element composition of the Spl websterite (a), protomylonite (b) and mylonite (c) whole-rocks and mineral cores and rims compiled from Tables 1 and 2. Plots and projections are computed with CSpace (Torres-Roldán *et al.*, 2000). It should be noted that pyroxenes from the Spl websterite are rich in the Tschermaks component and show minor core and rim variations (a) similar to the mylonite zone, where the cores and rims overlap yet plot close to the Al-free end-members (c). In contrast, pyroxenes from the protomylonite (b) span the whole compositional range, pointing to a continuous readjustment of the pyroxene composition during deformation. (d) Computed isochemical section for the protomylonite (RK139-5T) with calculated Al content of orthopyroxene (e) and modal amount of amphibole (f).

ultramylonitic part of the mylonite zone, clinopyroxene contains a small amount of structurally bound OH^-, as indicated by the characteristic peak at 3640 cm^{-1} (Fig. 10b). Quantification of the IR spectra shows that cores of clinopyroxene porphyroclasts contain higher amounts of structurally bound 'water' in the protomylonite and Spl websterite zones (729–818 ppm) than in the mylonite (675–692 ppm) (Fig. 10a, Table 3). In the porphyroclast rims and in the neoblasts intrinsic and extrinsic absorbance peaks overlap with the broad bands of submicroscopic fluid inclusions, preventing a straightforward quantification of structurally bound OH^- groups, which strongly depends on the subtraction of the fluid inclusion-related overlapping bands. The calculated water content based on these spectra is therefore only indicative, but the much lower water contents in neoblasts in the mylonite zone (~55 ppm) and in the porphyroclast rims in the mylonite and protomylonite zones (~276 ppm) may reflect a gradual decrease of structurally bounded OH^- towards the shear zone (Fig. 10b, Table 3).

Plagioclase exhibits highly variable absorbance spectra that are characterized by a broad band centered at

Table 3: Results of unpolarized light clinopyroxene FTIR measurements

Location of FTIR analysis			Technical details			FTIR data			
Micro-structural zone	Cpx type	Type of analysis	Aperture (μm)	Slab Thickness (μm)	1σ	*n*	$3 \times Abs_{av}$ (cm^{-2})	% NSI*	'Water' content (wt ppm H_2O)†
Spl webst.	porph.	core	80 × 80	159	11	13	5885	1	830
Protomyl.	porph.	core	80 × 80	148	9	16	5430	5	727
Protomyl.	neoblast	—	40 × 40	148	9	11	2089	30	206
Mylonite	porph.	core	80 × 80	166	10	10	5120	4	693
Mylonite	neoblast	—	40 × 40	166	10	11	2300	25	243
Ultramyl.	porph.	core	80 × 80	166	10	6	5021	5	673
Ultramyl.	neoblast	—	100 × 100	166	10	11	549	29	55

Abs_{av}, total integrated OH absorbance from average unpolarized spectra. OH contents calculated using extinction coefficients from Bell *et al.* (1995).
*Proportion of non-intrinsic separate inclusions (see Matsyuk & Langer, 2004) where NSI are 3710 and 3680 cm^{-1} peaks and correspond to amphibole inclusions.
†'Water' content exluding NSI. Uncertainty is less than 30%.

3440 cm^{-1} overlapping with two narrower peaks at *c.* 3400 cm^{-1} and 3280 cm^{-1} (Fig. 10c). The position of the narrow peaks is consistent with hydroxyl groups (Johnson, 2003; Johnson & Rossman, 2003, 2004) whereas the large variation in absorbance of the main broad band indicates the heterogeneous distribution of fluid inclusions in plagioclase.

Stress

Differential stresses during the formation of the dunite and granular pyroxenite can be estimated using experimentally derived dislocation creep flow laws for dry and wet olivine and clinopyroxene (Bystricky & Mackwell, 2001; Hirth & Kohlstedt, 2003; Chen *et al.*, 2006). Assuming fast mantle strain rates (10^{-14} and 10^{-12} s^{-1}) and temperatures ranging from 920 to 1005°C, dry olivine (8–85 MPa) is five times weaker than dry clinopyroxene (35–275 MPa), especially at the lowest temperatures. Under water-saturated conditions stress estimates are, however, similar for both phases, in the range of 1–18 MPa, consistent with the proposal of Chen *et al.* (2006) that water-saturated clinopyroxenite may be weaker than wet peridotite.

Alternative stress estimates may be provided by recrystallized grain size paleopiezometry; however, there is currently no consensus as to whether the recrystallized grain size is a function of stress or of deformational work (Austin & Evans, 2007; Rozel *et al.*, 2011). This method also depends highly on the relation between the dislocation density and stress, therefore it is only valid for dislocation creep. In the mylonite zone, the paleopiezometer of Twiss (1977) was applied to estimate the stresses that might have resulted in dynamic recrystallization of olivine and plagioclase in the 7–50 μm grain-size range. Although various criticisms have been raised concerning the applicability of this simple grain-size piezometer (e.g. Twiss & Sellars, 1978; De Bresser *et al.*, 2001; Shimizu, 2008) and the fact that, being based on deformation by dislocation creep, it is not applicable to very fine-grained aggregates, where diffusion and grain boundary sliding may play an important role, this method returns values in the range 110–430 MPa and 60–200 MPa for olivine and plagioclase, respectively, which correlate well with the stress range calculated for the coarse-grained microstructural zones. These values may therefore represent the maximum stresses in these domains.

DISCUSSION

Deformation mechanisms

Well-developed CPOs (Fig. 5a–d), high frequencies of correlated low-angle misorientations of neighboring grains (Fig. 6c and d), moderate J-indices (Fig. 4c), and the non-random distribution of crystallographic axes (Fig. 6a and b) indicate that plastic deformation of olivine and clinopyroxene in the dunite and Spl websterite zones occurred by dislocation creep (Randle, 1993; Tommasi *et al.*, 1999; Wheeler *et al.*, 2001; Soustelle *et al.*, 2010; Vauchez *et al.*, 2012). The protomylonite zone shows similar characteristics, suggesting that dislocation creep was also the dominant mechanism in this zone, but the occurrence of strain-free neoblasts, the weaker crystallographic fabric (Fig. 4c) and increasing tendency of low-angle correlated misorientations towards random distribution (Fig. 6c) may indicate that grain-size sensitive (GSS) deformation

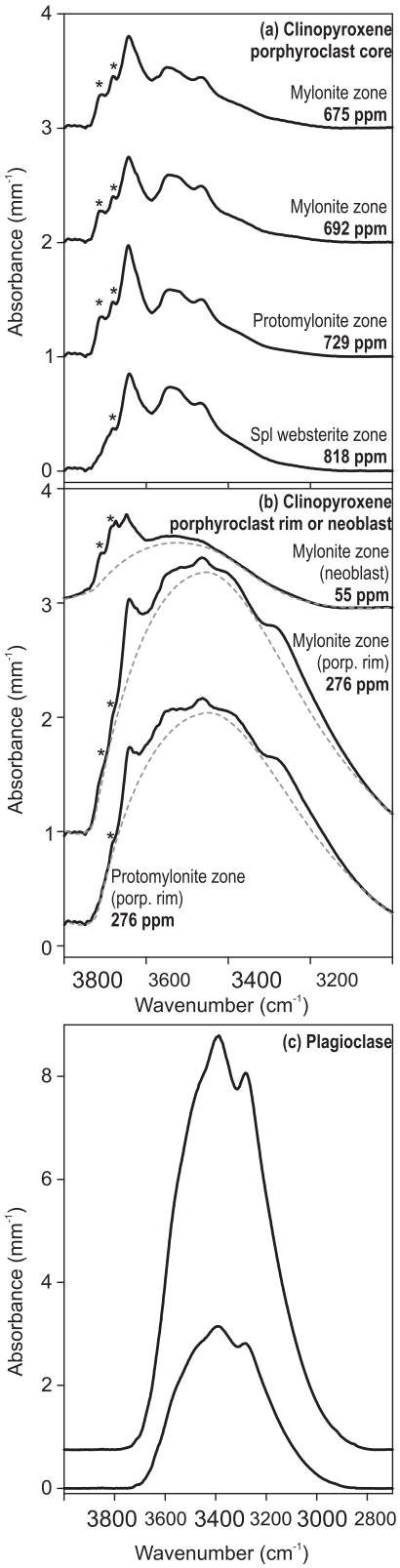

Fig. 10. Normalized average unpolarized FTIR spectra for cores of clinopyroxene porphyroclasts (a), rims of clinopyroxene porphyroclasts and clinopyroxene neoblasts (b), and plagioclase (c) in the various microstructural zones. Dashed lines in (b) indicate the proposed baseline owing to molecular water in fluid inclusions, which has been used for the estimation of the concentration of OH-related bands. Plagioclase exhibits highly variable absorbance spectra and (c) illustrates two end-members of all the spectra taken on this mineral. Asterisks in (a) and (b) correspond to pargasite- and/or tremolite-related peaks.

mechanisms also accommodated some of the deformation. We suggest that this latter deformation mechanism is dominant in the fine-grained olivine-rich domains produced by the spinel to plagioclase phase transformation reaction. The correlation between olivine [100] and clinopyroxene [001], and the alignment of these axes subparallel to the lineation (Fig. 5) indicate that [100] in olivine and [001] in clinopyroxene are the dominant slip directions. Further information on the active slip systems in the dunite and in the coarse-grained pyroxenite zones may be derived from the analyses of rotation axes accommodating low-angle misorientations within crystals and the relative concentration of the three main crystallographic axes (Soustelle *et al.*, 2010; Frets *et al.*, 2012). Rotation axes within olivine single grains show a girdle-like distribution from [001] to [010] (not shown), and the relative concentration of [010] and [001] axes—defined as the ratio of maximum concentration of the two axes—shows the dominance of [010]. These observations suggest principal slip of olivine on the (010) plane in all zones except the protomylonite, where the similar concentration of [010] and [001] axes indicates equal activation of these two planes in olivine. All these observations are consistent with subgrain boundaries formed by $\{0kl\}[100]$ edge dislocations in olivine, with a predominance of (010) or (001) planes at moderate to high temperatures (800–1000°C; e.g. Carter & Avé-Lallemant, 1970) and low to moderate water contents (Jung & Karato, 2001).

As shown above, the correlation between clinopyroxene and olivine CPO (Fig. 5a–d) indicates consistent deformation of these mineral phases, with the activation of the [001] slip direction in clinopyroxene. However, rotation axes accommodating low-angle misorientations in clinopyroxene crystals have a clear maximum around [001] that seems inconsistent with the [001] slip direction (not shown). In plastically deformed pyroxene in high-temperature (~1150°C) spinel websterites, Frets *et al.* (2012) have reported the same rotation axes in clinopyroxene and interpreted them to result from accumulation of dislocations along deformation twins on the (100) plane, producing further rotations around [001] that transform the twin lamellae into subgrains. The same mechanism may account for the unusual rotation axes around [001] observed in clinopyroxenes in our samples, where mechanical twinning is widespread. Hence, clinopyroxene

in dunite and Spl websterite records deformation encompassing mechanical twinning on (100)[001] and dislocation glide, assisted by dynamic recrystallization and subgrain rotation. The observed clinopyroxene CPO is consistent with dominant activation of the {110}[001] slip systems (Bascou *et al.*, 2002).

Compared with dunite and coarse-grained pyroxenite zones, olivine and clinopyroxene in the mylonite, especially in the ultramylonitic bands, exhibit (1) significantly weaker CPO (Fig. 5e and f) and weak J-indices (Fig. 4c), (2) a dominantly random distribution of all crystallographic axes examined based on eigenvalue analyses (Fig. 6a and b), (3) misorientation histograms that differ from the theoretical random distribution only by a small peak at correlated misorientations <30° (Fig. 6c and d), and (4) random distribution of rotation axes accommodating low-angle misorientations within the crystals. Among these observations the weak CPO and the misorientation histogram suggest that dislocation creep occurred, but these data provide a weak basis to reconstruct active slip systems. Olivines are elongated and their [001] and [100] axes are distributed on a girdle with [100] maxima roughly subparallel to lineation, suggesting dominant activation of dislocations with [100] Burgers vectors. In clinopyroxene, the fact that maxima of (010) planes are perpendicular to the foliation and [001] axes are subparallel to the lineation may indicate the activation of {110}[001] slip systems. However, the very fine grain size (Fig. 4b), the weak CPO (Fig. 5e and f) and the alignment of grain boundaries converge towards a major contribution of GSS mechanisms to the deformation.

GSS creep is theoretically expected to be favored by small grain sizes, low strain rates and/or low stresses and high temperatures (Etheridge & Wilkie, 1979; Tullis & Yund, 1985; Rutter & Brodie, 1988; Handy, 1989; Fliervoet & White, 1995; Ter Heege *et al.*, 2002; Hirth & Kohlstedt, 2003; Warren & Hirth, 2006; Platt & Behr, 2011; Bercovici & Ricard, 2012). However, many studies on natural shear zones have proposed that GSS creep predominates in low-temperature mylonites (e.g. Drury *et al.*, 1991, and references therein). To resolve this apparent contradiction, a widely accepted model—based on extrapolation of flow laws derived from high-temperature and high-stress experimental data (e.g. Braun *et al.*, 1999, and references therein)—proposes that grain-size reduction by dynamic recrystallization promotes a transition in dominant deformation mechanism from dislocation creep to GSS creep and that low temperature hinders grain growth (owing to the strong dependence of diffusion rates on temperature), allowing the system to remain in the GSS field. At high temperatures, fast diffusion rates favor grain growth and small grain sizes may be preserved only through Zener pinning (Bercovici & Ricard, 2012, and references therein).

In this study we observe that the switch from dislocation creep to GSS creep is accompanied not only by a sudden decrease of grain size (Fig. 4b) but also by the occurrence of plagioclase and amphibole (hydration) (Fig. 4a) in a decompressing and cooling system. All these factors—decrease in temperature during deformation, the fine-grained reaction products that may result in effective grain boundary pinning, and the hydration of the system—may effectively weaken the rock. Below we will evaluate their contribution to strain localization.

Constraints from numerical modeling

To better understand the interrelationship between the change in modal composition, the decrease of grain size and the switch in deformation mechanism, we performed one-dimensional (1D) numerical experiments in simple shear at constant stress (summarized in Tables 4 and 5). Given that empirical laws relating grain size to work rates and grain growth parameters are not available for pyroxenes, it is not possible to model directly the grain-size evolution and strain localization in a system similar to the one studied here. Therefore, we focused on the effect of viscosity contrast on strain localization by changing grain size, water content and modal composition according to the observations in the different microstructural zones of the studied sample. Our model is composed of a pyroxenite layer hosted in a coarse-grained dunite, where the pyroxenite layer itself consists of three subzones: Spl pyroxenite, Spl–Plag pyroxenite and fine-grained Plag–Spl pyroxenite. The mineral volume fractions and grain sizes of the different zones of the model setup (Table 4) roughly correspond to our observations on the dunite, the Spl websterite, protomylonite and the ultramylonite bands in the mylonite microstructural zones, respectively (Fig. 4a). In each setup, the diffusion of water, phase transformations and the time of evolution are neglected and the subdomains do not interact with each other.

The 1D models were run at a pressure of 0·9 GPa for a temperature range of 850–1000°C using constant stresses estimated previously for dry and wet olivine and clinopyroxene rheologies. Three situations were modeled as follows. To monitor the effect of extreme cases, a fully dry setup with completely dry dunite and dry pyroxenite rheologies and a fully wet setup with water-saturated dunite and pyroxenite rheologies were used. Based on the available analytical data (Tables 3 and 5; see Fig. 10) a more realistic setup was compiled with a dry dunite, a wet Spl websterite, and protomylonite and mylonite zones with intermediate water contents. Further details of the numerical experiments are given in Appendix B.

In all setups, the mylonite accommodates the fastest strain rates and it is the only subdomain where dislocation creep is not dominant (Fig. 11). In the fully dry setup the dunite and the protomylonite have comparable strain rates (Fig. 11a1 and a2), and the Spl websterite is the most

Table 4: Mineral volume fractions and grain sizes used for the numerical modeling

	Dunite		Spl webst.		Protomylonite		Mylonite	
	vol. %	Grain size (μm)	vol. %	Grain size (μm)	vol. %	Grain size (μm)	vol. %	Grain size (μm)
Pyroxenes	0·12	1731	0·77	2683	0·73	2944	0·60	4·4
Spinel	0·06	1644	0·11	1488	0·08	1185	0·05	3·1
Plagioclase	0·00	—	0·00	—	0·08	397	0·20	4·8
Olivine	0·82	4095	0·12	1034	0·11	825	0·15	3·7

'Pyroxenes' include both orthorhombic and monoclinic pyroxenes.

Table 5: Rheologies used for the various model setups

	Dunite			Spl websterite			Protomylonite			Mylonite		
	Full-DRY	Full-WET	REAL	Full-DRY	Full-WET	REAL	Full-DRY	Full-WET	REAL	Full-DRY	Full-WET	REAL
Pyroxenes	DRY	WET	*DRY*	DRY	WET	*WET*	DRY	WET	*SEMI*	DRY	WET	*DRY*
Spinel	DRY	DRY	*DRY*	DRY	DRY	*DRY*	DRY	DRY	*DRY*	DRY	DRY	*DRY*
Plagioclase	—	—	—	—	—	—	DRY	WET	*WET*	DRY	WET	*WET*
Olivine	DRY	WET	*DRY*	DRY	WET	*WET*	DRY	WET	*WET*	DRY	WET	*WET*

SEMI, 50–50% mixture of wet and dry rheology. Rheologies used for dislocation creep and diffusion creep, respectively: olivine from Karato & Jung (2003) and Hirth & Kohlstedt (2003); pyroxenes from Chen *et al*. (2006) and Hier-Majumber *et al*. (2005); plagioclase from Rybacki & Dresen (2004) and Rybacki *et al*. (2006); spinel from Lawlis *et al*. (2001).

resistant zone of the model (Fig. 11a3), indicating that even low modal contents of dry plagioclase are able to significantly weaken bulk-rock rheology. However, water-saturated pyroxenes are significantly weaker than dry ones and their rheology becomes comparable with that of wet olivine (Chen *et al.*, 2006). Thus in the fully wet setup all the coarse-grained microstructural zones from the dunite to the protomylonite are characterized by similar strain rates (Fig. 11b1–3). Nonetheless, strain rates in this setup (Fig. 11b) are at least two orders of magnitude larger than in the dry setup (Fig. 11a) and the plagioclase-bearing subdomain shows the largest strain rates. This observation suggests that occurrence of wet plagioclase (Fig. 11b3) further weakens the bulk rheology even under water-saturated conditions. In the realistic model setup the pyroxenite layers (Fig. 11c2 and c3) are weaker than the dunite (Fig. 11c1), the water-saturated Spl websterite and the protomylonite showing similar strain rates (compare Fig. 11c2 and c3; see also Fig. 11d), which can be explained only by the buffering effect of newly formed wet plagioclase and olivine. These reaction products introduce significant weakening to the rock that may balance the gradual hardening of pyroxene porphyroclasts, the latter being a consequence of dehydroxylation shown by decreasing 'water' contents towards the mylonitic shear zone (Fig. 10a). The numerical modeling also shows that the fine-grained reaction products deform mainly by GSS deformation (diffusion creep). However, neither the weaker rheology nor the small grain size can result in strain localization alone. Dramatic increase of strain rate in the protomylonite zone is observed when the modal amount of the reaction products exceeds a certain threshold, highlighting the role of the spinel to plagioclase phase transformation reaction in localizing strain.

Ductile strain localization: why in pyroxenite?

Causes of strain localization

Ductile strain localization may be triggered by the following factors: (1) the presence of fluids or melts (Bauer *et al.*, 2000; Burg & Vigneresse, 2002; Vigneresse & Burg, 2004); (2) boundary conditions (constant stress boundary conditions favor localization; Hansen *et al.*, 2012); (3) temperature heterogeneity owing to shear heating (Ogawa, 1987;

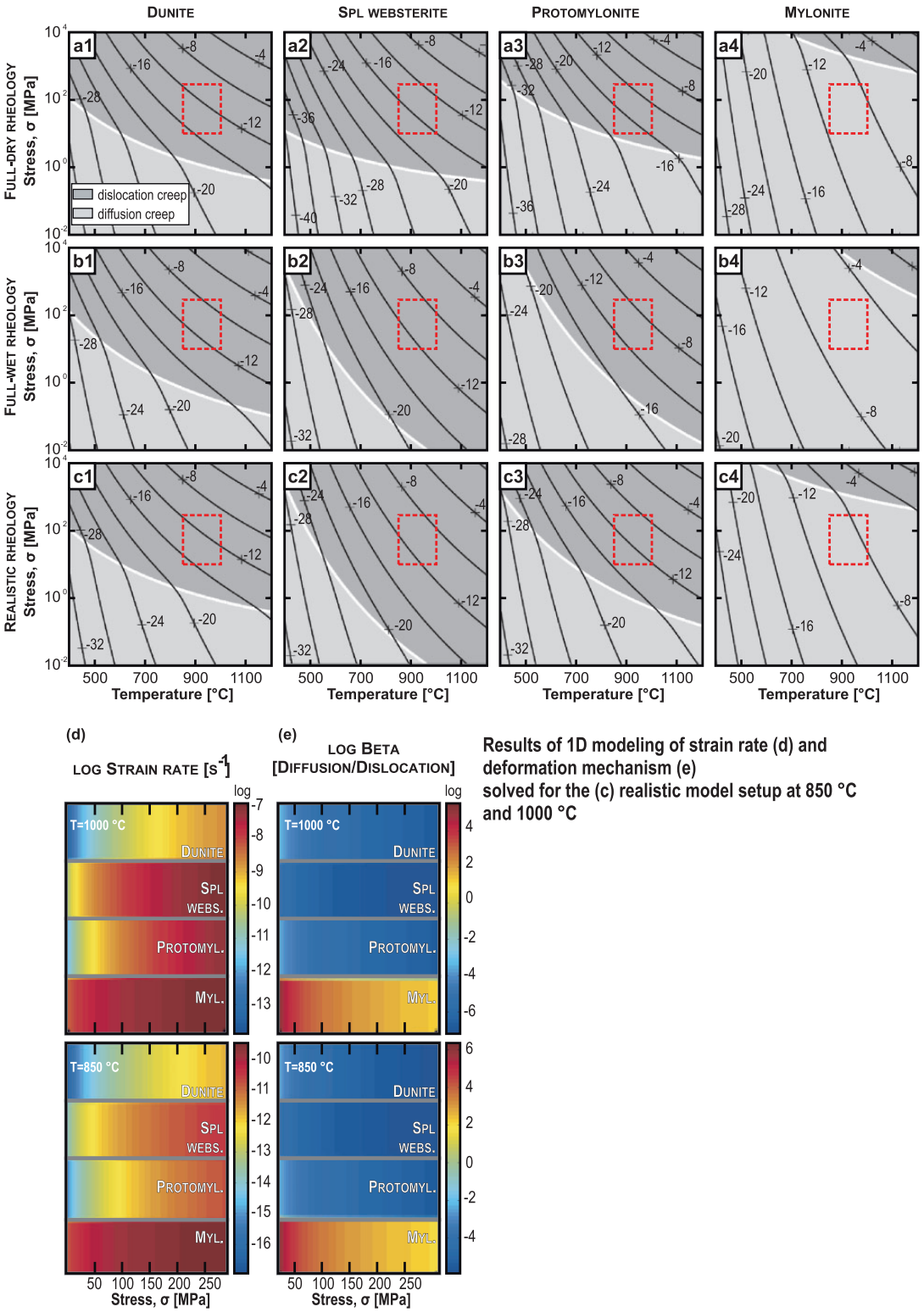

Results of 1D modeling of strain rate (d) and deformation mechanism (e) solved for the (c) realistic model setup at 850 °C and 1000 °C

Fig. 11. Deformation maps of dunite, Spl websterite, protomylonite and mylonite zones (from left to right) calculated for full-dry (a1–a4), full-wet (b1–b4) and realistic (c1–c4) rheologies. Model setup and parameters used for the numerical calculations are summarized in Tables 4 and 5. (d, e) Results of modeling the strain rate (d) and deformation mechanism (e) across the microstructural zones of the realistic model setup at 850°C (bottom) and 1000°C (top). Beta is expressed as the ratio of the diffusion creep/dislocation creep strain rates, where the higher the value, the more diffusion creep there is. Red dashed square outlines the estimated temperature and stress range of the studied samples.

Regenauer-Lieb *et al.*, 2001; Thielmann & Kaus, 2012); (4) switches in deformation mechanism owing to textural evolution (Poirier, 1980; Schmid, 1982; Drury *et al.*, 1991), including grain-size reduction (Braun *et al.*, 1999; Molli *et al.*, 2000); (5) inherited rheological features such as textural heterogeneity and anisotropy (Vilotte *et al.*, 1984; Tommasi *et al.*, 1995, 2009; Tommasi & Vauchez, 2001; Neves *et al.*, 2008); (6) intrinsic rock properties and/or their modification under applied stress and/or synkinematic, as when (net-transfer) reactions are triggered (Furusho & Kanagawa, 1999; Newman *et al.*, 1999; Stünitz & Tullis, 2001; de Ronde *et al.*, 2004; Vauchez *et al.*, 2012); or (7) some combination of the above.

In the present study, textural evidence (Figs 2 and 3) and major element compositions (Fig. 7b and d; Table 2) suggest that formation of the localized mylonitic shear zones is closely linked to phase transformation reactions during cooling and decompression. Thus we infer that shear heating had a negligible influence on strain localization. In addition, the spinel to plagioclase phase transformation reaction has a positive Clapeyron slope and the lower-pressure assemblage is characterized by higher molar entropy (Asimow *et al.*, 1995). This reaction is thus endothermic, which is consistent with our geothermobarometric data that indicate cooling (Fig. 7b and d). Numerical experiments also show that localization is more likely to take place during cooling, especially if deformation is coeval with cooling (Braun *et al.*, 1999). However, ductile strain localization in pyroxenite controlled solely by cooling is not supported by our data because evidence for temperature decrease was identified in all zones, but strain localization is restricted to the mylonite, where the modal amount of plagioclase, secondary olivine and amphibole is the highest (Table 1; Figs 3e–i and 4a).

Plagioclase and secondary olivine are the products of the spinel to plagioclase phase transformation reaction. The size of these new, strain-free phases is significantly smaller than the average grain size in the protolith (Fig. 3d and e) and their modal abundance gradually increases towards the mylonite (Fig. 4a). Extreme grain-size reduction (2–25 μm) in polymineralic peridotite ultramylonites has been previously suggested to result from continuous net-transfer reaction related to the spinel to plagioclase phase transition (Furusho & Kanagawa, 1999; Newman *et al.*, 1999; Kaczmarek & Tommasi, 2011). These fine-grained polymineralic aggregates around porphyroclasts hinder grain growth owing to pinning and allow a switch from dislocation creep in porphyroclasts to GSS creep in the fine-grained matrix. Nevertheless, the phase transformation reaction is unlikely to lead to strain localization if it is not synkinematic. Multipolar Al–Cr zoning in spinel is regarded to be a result of stress-induced chemical diffusion (Ozawa, 1989) and the preservation of such zoning in plagioclase-rimmed spinels in lherzolites has been cited as evidence for the formation of plagioclase under stress, as postkinematic formation of plagioclase would have destroyed the multipolar zoning by selectively consuming Al at the long tips of spinel (Furusho & Kanagawa, 1999). In the studied Ronda pyroxenite, the preservation of this zoning in both the plagioclase-bearing and plagioclase-free websterite zones (Fig. 8) leads to a similar conclusion, indicating that plagioclase crystallization is synkinematic. Moreover, the presence of amphibole among the reaction products and its increasing modal abundance towards the mylonitic shear zone (up to 1·0–1·5 vol. %) (Fig. 4a) suggests that hydrous pore fluids may have assisted both the phase transformation reaction and strain localization.

Water-derived species structurally bound as OH^- in crystal defects are primary players in the weakening of nominally anhydrous minerals (NAMs) (Chen *et al.*, 2006; Kohlstedt, 2006; Hirschmann & Kohlstedt, 2012), whereas molecular water-rich pore fluids have a pronounced kinetic effect in catalyzing reactions (Blacic & Christie, 1984; Rubie, 1986). In the studied zone, clinopyroxene cores display a gradual decrease of hydroxyl contents towards the plagioclase-bearing mylonitic zone (Fig. 10a and b; Table 3). Thus if strain localization in the pyroxenite resulted only from structurally bound OH^- in the clinopyroxene, it should have occurred in the wet Spl websterite zone. On the other hand, amphibole occurs as rims around plagioclase and clinopyroxene (Fig. 2e), indicating that its formation is coeval with the phase transformation reaction and strain localization. The modal amount of amphibole is too low to form interconnected layers within the rock (Fig. 3d–i) and its sole presence is thus unlikely to localize strain. However, the crystallization of amphibole and the existence of submicrometre fluid inclusions in the clinopyroxene rims (Fig. 10b) suggest that strain localization happened in the presence of pore fluids. Recent experiments on wet olivine polycrystals (Demouchy *et al.*, 2012) showed a clear strain softening associated with the presence of a hydrous pore fluid at grain boundaries during deformation, confirming earlier interpretations by Chopra & Paterson (1984). Moreover, hydrous pore fluids probably catalyzed the phase transformation reaction and increased reaction rates. The free fluid was partly incorporated in the newly formed plagioclase and secondary olivine and was partially consumed by the crystallization of amphibole by replacing clinopyroxene and plagioclase rims (Fig. 2d and e), resulting in the hydration of the reaction products (Fig. 10c). We propose therefore that the fluids played an important role but that the primary factor leading to strain localization was the viscosity contrast introduced into the rock by the reduced grain size of hydrated plagioclase and secondary olivine formed during the spinel to plagioclase phase transformation reaction.

Conceptual model for strain localization

A possible scenario accounting for strain localization in the studied pyroxenite involves grain-size reduction and coupled changes in the deformation mechanisms as a result of the spinel to plagioclase phase transformation reaction, which first occurred and culminated in the more Al-rich pyroxenite owing to its more fertile composition. To explain the presence of amphibole, this model would make use of the classical concept of fluid channeling along shear zones, where pore fluids arrive from an external source in an open system and provide positive feedback for the deformation (Etheridge *et al.*, 1983; Selverstone *et al.*, 1991*l*; Oliver, 1996; Mahan *et al.*, 2006). Whereas in metamorphic rocks the external fluids can be expelled from either the overlying or the underlying—typically originally sedimentary—units, in the deep lithosphere their origin is usually explained by melt–fluid immiscibility (Roedder, 1992). There is clear evidence in Ronda for partial melting in the granular spinel peridotite domain (Van der Wal & Bodinier, 1996; Lenoir *et al.*, 2001*l*), but observations indicate that it produced silicate melts in which H_2O is highly soluble (King & Holloway, 2002; Botcharnikov *et al.*, 2005; Hidas *et al.*, 2010). Even though the melt would have crystallized by the time the mylonite zone formed, releasing the dissolved water, it is unlikely that this produced water-rich pore fluids by immiscibility, as would be required to form amphibole. The classical model of fluids channeling by shear zones also does not explain many characteristics of the studied pyroxenite shear zone. Specifically, this model fails to (1) answer why amphibole occurs only in the plagioclase-bearing protomylonite and mylonite zones, and (2) explain why the cores of clinopyroxene porphyroclasts show decreasing hydroxyl contents towards the mylonite, if the mylonitic shear zone is the most fluid-impregnated area (Fig. 10a, Table 3).

Our data support an alternative scenario in which weakening initiated with the phase transformation reaction, leading to ductile strain localization in a (quasi-)closed system with the help of several interdependent factors. Figure 12 shows a schematic illustration of the proposed conceptual model for strain localization in plagioclase facies pyroxenite. At high temperature in the spinel lherzolite facies (t1 in Fig. 12a and b), coarse-grained dunite and pyroxenite deformed by dislocation creep (Fig. 11e) producing the observed CPO (Fig. 5a and b) and coarse-grained porphyroclastic microstructures with few neoblasts (Figs 2a, b and 3a–c). The presence of stress-induced anisotropic Cr–Al zoning in spinel (Ozawa, 1989) from the Spl websterite zone (Fig. 8a–c) indicates that there was an anisotropic stress field during the high-temperature deformation stage (t1 in Fig. 12a and b). During uplift, at around 0·6–0·8 GPa pressure (Fig. 9e), the spinel to plagioclase reaction (Fig. 12b, t2) induced a substantial decrease in the Al content of the pyroxenes (Fig. 7) and, as aluminum is known to greatly enhance hydroxyl solubility in orthopyroxene (Mierdel *et al.*, 2007) and clinopyroxene (Gavrilenko & Keppler, 2007; Gavrilenko, 2008), this loss led to hydrogen extraction (Fig. 10a and b; Table 3), *in situ* release of a fluid phase and crystallization of amphibole (Fig. 2d and e), wet plagioclase (Fig. 10c) and fine-grained, secondary olivine (compare Fig. 12a and b, t1 and t2). Alternatively, as the Al content of clinopyroxene in the spinel facies mostly depends on the temperature at which equilibrium occurs (Gasparik, 1984, 1987), if cooling had occurred prior to strain localization, it might have led to the release of minor amounts of fluid that started and catalyzed the spinel to plagioclase phase transformation reaction. In either case, the free fluid phase enhanced grain boundary diffusion, enhanced reaction rates (Rubie, 1986) and catalyzed the progress of reaction. Enhanced anisotropic Cr–Al zoning in spinels rimmed by plagioclase neoblasts in the protomylonite and mylonite zones (Fig. 8d–i) indicates synkinematic formation of plagioclase (Furusho & Kanagawa, 1999).

Partitioning of water from minerals to a fluid phase or melt during pressure-release dehydration has been proposed to effectively dry out the mantle as it upwells beneath mid-ocean ridges, leading to an increase in strength (Hirth & Kohlstedt, 1996). Given that the mechanical strength of dry (i.e. less hydrated or 'water'-poor) pyroxene is higher than that of the wet (Bystricky & Mackwell, 2001; Chen *et al.*, 2006; Bürgmann & Dresen, 2008), hydrogen extraction from pyroxenes as a result of Al loss during the spinel to plagioclase reaction should lead to hardening of the pyroxene porphyroclasts in the protomylonite with respect to those in the Spl websterite protolith (compare Fig. 11b and Fig. 11a), counteracting strain localization in this layer. However, the results of our numerical model point to an alternative evolution in a closed system because, at the rock scale, the crystallization of fine-grained neoblasts of wet plagioclase and of secondary olivine may compensate the hardening, resulting in similar strain rates in the Spl websterite and the protomylonite zone (Fig. 11c2, c3 and d). The net-transfer reaction produces a heterogeneously distributed weak phase assemblage in the pyroxenite, resulting in a progressively increasing viscosity contrast between hardened porphyroclasts and weak neoblasts. The fine-grained reaction products also permit a switch in the deformation mechanism from dislocation creep to GSS creep (Fig. 11e), allowing for further weakening of the mylonite zone (Fig. 11c and d).

We propose that ductile strain localization is primarily a result of the spinel to plagioclase reaction under stress and the key to localization resides in the progress of the net-transfer reaction, which, at a certain point, results in the products forming interconnected weak layers (Handy *et al.*, 1999). In the studied pyroxenite, strain localization

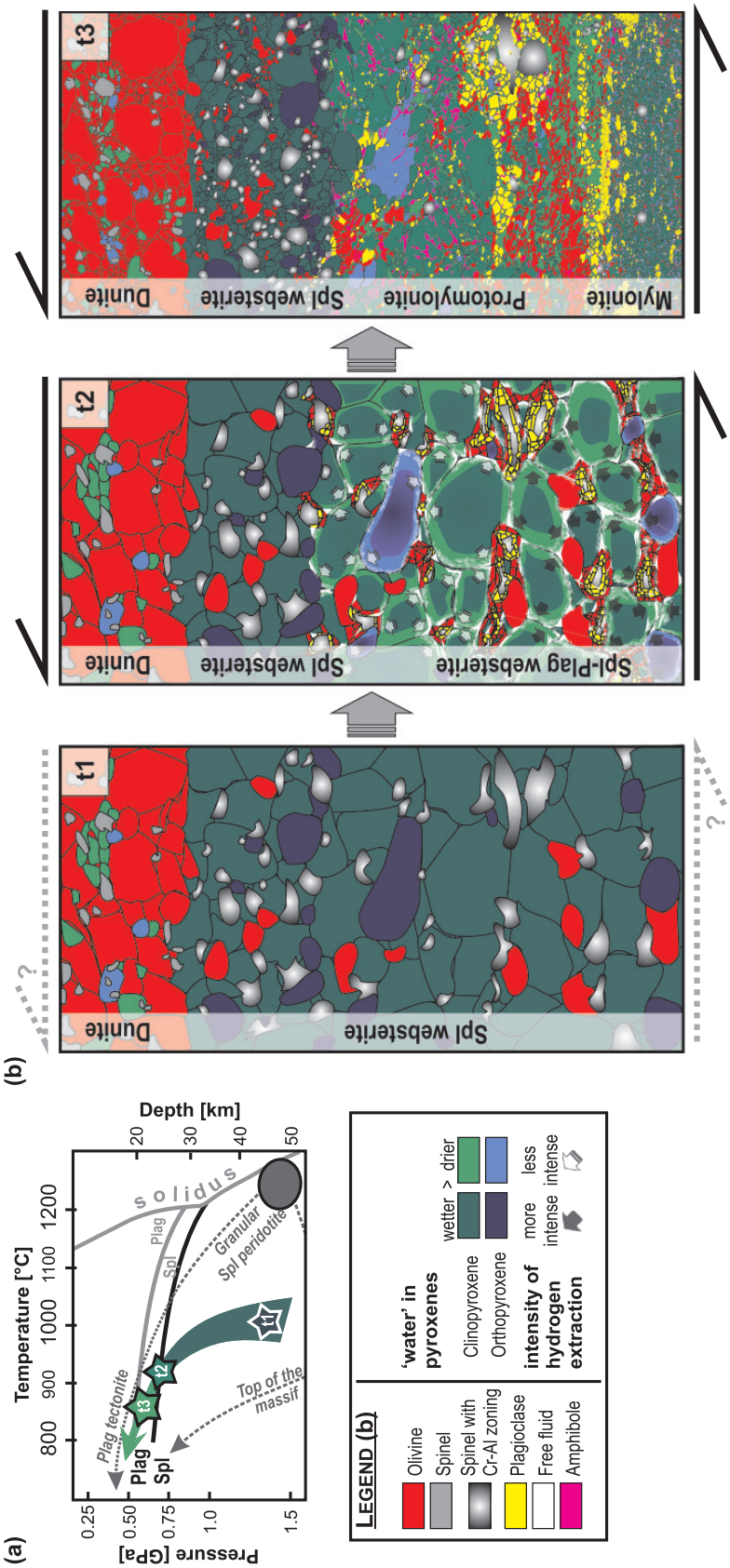

Fig. 12. Conceptual model for softening and strain localization in the studied Ronda pyroxenite. (a) Approximate P–T–t path of the studied samples presented as a snapshot at t1 (oldest), t2 and t3 (youngest) in (b). Dotted grey lines in (a) indicate the P–T path of the Ronda Massif after Garrido *et al.* (2011). Continuous grey lines indicate the spinel to plagioclase facies transition and solidus in fertile lherzolite. Continuous black line denotes the spinel–plagioclase phase transition in pyroxenite (Schmädicke, 2000). (b) Microstructural and modal evolution of the dunite and pyroxenite zones during softening that led to strain localization. All of t1–t3 represent approximately the same rock volume. (See text for further details.)

was achieved in the center of the layer (Fig. 12b, t3) owing to either its more fertile whole-rock composition with respect to the Spl websterite zone (Figs 4d and 9) or the first occurrence of free water during the hydrogen extraction from clinopyroxene that further fueled the phase transformation reaction. We suggest that sudden grain-size reduction (Fig. 4b) and the switch in the deformation mechanism from dislocation to GSS creep in the mylonite zone is a consequence of strain localization that was triggered by the spinel to plagioclase facies net-transfer reaction.

Role of pyroxenites in strain localization during thinning of the shallow subcontinental lithospheric mantle

Synkinematic net-transfer reaction, such as the breakdown of spinel to plagioclase, is an effective cause of weakening and strain localization in the shallow lithospheric mantle (Furusho & Kanagawa, 1999; Newman *et al.*, 1999). Because plagioclase is stable at higher pressures in fertile rocks (Borghini *et al.*, 2010), this reaction occurs deeper in clinopyroxene-rich pyroxenite than in peridotite (e.g. Schmädicke, 2000) (Fig. 4d). Consequently, during extension of the subcontinental lithospheric mantle, the spinel to plagioclase reaction takes place first in pyroxenite. Compositional variations, such as pyroxenite layers, also constitute rheological heterogeneities that may induce heterogeneous weakening during deformation and strain localization (e.g. Drury *et al.*, 1991; Treagus & Sokoutis, 1992; Toy *et al.*, 2010; Vauchez *et al.*, 2012).

Our study area is situated at the transition from the overlying granular spinel peridotite to the underlying plagioclase tectonite domain (Fig. 1), which records the latest ductile evolution of the Ronda Peridotite before its emplacement in the crust (Van der Wal & Vissers, 1996; Hidas *et al.*, 2013). Here, mylonitic shear zones occur mostly in thin pyroxenites; however, down-section, shear zones become progressively wider and propagate into the host peridotite. Peridotitic and pyroxenitic shear zones exhibit a clear NNE-dipping foliation and NE–SW-trending lineation, and record top-to-the-south or -SW sense of shear. Hidas *et al.* (2013) proposed formation of these shear zones in the latest ductile evolution of the Ronda Peridotite during kilometer-scale folding and synkinematic shearing of the lithospheric mantle, related to the uplift of the massif from the spinel to plagioclase lherzolite facies, leading to final emplacement in the crust. According to those researchers, the Ronda plagioclase tectonite domain represents the axial surface of a fold that evolved synchronously with the mylonitic shear zones. The observed strain localization in fertile pyroxenite occurred during this tectono-metamorphic stage during decompression. Thus whereas the host peridotite ductile foliations and lineations show orientations, which indicate that it formed synchronously to those in the older, overlying spinel tectonite domain (see Darot, 1973; Precigout *et al.*, 2007; Soustelle *et al.*, 2009), the studied pyroxenite shear zone records the same kinematics as the peridotitic mylonites in the underlying, younger plagioclase tectonite domain (Hidas *et al.*, 2013). These structural similarities and the decoupling between high-temperature peridotite and lower-temperature mylonite foliations indicate that the studied outcrop must have been developed at a transitional stage, postdating the spinel tectonite foliation but pre- to synkinematic to the plagioclase tectonites. The progressive widening of pyroxenite shear zones towards the base of the massif (Fig. 1a–e), the strong structural correlation in the kinematics of peridotitic and pyroxenitic shear zones (inset in Fig. 1b), and the deeper stability of plagioclase in fertile rocks (Borghini *et al.*, 2010) point towards the conclusion that during the final stages of uplift ductile strain localization occurred first and deepest in the most fertile rock types, represented by the studied Plag–Spl pyroxenites. Narrow, pyroxenite-hosted shear zones became wider towards the base of the subcontinental lithospheric mantle section and may have propagated out to the surrounding peridotites as well, and these wide peridotite shear zones then contributed to the exhumation of the largest outcrop of subcontinental lithospheric mantle on Earth (i.e. the Ronda Peridotite). Thus, strain localization in pyroxenite can be the cradle of intralithospheric weak zones in various geodynamic settings, such as in back-arcs where upwelling of upper mantle material is expected to occur.

CONCLUSIONS

Pyroxenite mylonites demonstrate that weakening was achieved by the spinel to plagioclase facies reaction, assisted and catalyzed by water-rich pore fluids. Reaction caused grain-size reduction and hindered subsequent grain growth, allowing for effective weakening of the most fertile layers—the pyroxenites. Microstructural analyses show that deformation of the mylonite aggregate occurred by grain-size sensitive mechanisms in contrast to the coarse-grained porphyroclasts that deformed by dislocation creep.

The synkinematic net-transfer reaction was assisted by the release of fluids probably formed by hydrogen extraction from clinopyroxene that catalyzed the phase transformation reaction and resulted in wet reaction products (fine-grained olivine and plagioclase). The whole-rock major element composition of the studied pyroxenite and thermodynamic modeling using Perple_X indicate that the phase transformation took place at deeper levels than in the fertile peridotites. This suggests that pyroxenites might play an important role in hosting lithospheric scale shear zones during thinning of the subcontinental lithospheric mantle, as initial strain localization at deeper levels may propagate out from thin pyroxenite layers into larger shear zones that also affect mantle peridotites.

ACKNOWLEDGEMENTS

The authors acknowledge the thorough and constructive reviews by Masaaki Obata, John Platt and Virginia Toy, as well as the careful editorial work of Executive Editor Marjorie Wilson, which substantially improved the paper. We are indebted to J. Hermann for fruitful discussions, which motivated us to carry out the measurements of pyroxene 'water' content. The authors owe thanks to I. Guerra-Tschuschke (CIC, Universidad de Granada, Spain) for skilful acquisition of EDS-VP-SEM chemical maps, and R. Reyes-González (IACT, CSIC-UGR, Spain) for sample preparation and thin section polishing. We also acknowledge the help of M. A. Hidalgo Laguna (CIC, Universidad de Granada, Spain) and X. Llovet (CCiTUB, University of Barcelona, Spain) during EPMA sessions, and the assistance of F. Barou (Géosciences Montpellier, UM-2, France) during EBSD mapping.

FUNDING

This research benefited from several grants and fellowships funded by the European Fund of Regional Development. This work was supported by the International Lithosphere Program (grant CC4-MEDYNA to C.J.G.), the Spanish Ministry of Economy and Competitiveness (MICINN) (grant CGL2010-14848 to C.J.G.), the Junta de Andalucía (grants RNM-131 and 2009RNM4495 to C.J.G. and post-doctoral fellowship to K.H.), the European Union Framework Programme 7 (EU-FP7) Marie Curie postdoctoral grants (PIOF-GA-2010-273017 to J.A.P.N., PIEF-GA-2008-220664 to C.M.), and funding from the Initial Training Network (ITN) Crystal2Plate, an FP7-funded Marie Curie Action under grant agreement number PITN-GA-2008-215353 to E.F. and M.T.

SUPPLEMENTARY DATA

Supplementary data for this paper are available at *Journal of Petrology* online.

REFERENCES

Amelinckx, S. & Dekeyser, W. (1959). The structure and properties of grain boundaries. In: Frederick, S. & David, T. (eds) *Solid State Physics*. Academic Press, pp. 325–499.

Asimow, P. D., Hirschmann, M. M., Ghiorso, M. S., O'Hara, M. J. & Stolper, E. M. (1995). The effect of pressure-induced solid–solid phase transitions on decompression melting of the mantle. *Geochimica et Cosmochimica Acta* **59**, 4489–4506.

Austin, N. J. & Evans, B. (2007). Paleowattmeters: A scaling relation for dynamically recrystallized grain size. *Geology* **35**, 343–346.

Baker, M. B. & Stolper, E. M. (1994). Determining the composition of high-pressure mantle melts using diamond aggregates. *Geochimica et Cosmochimica Acta* **58**, 2811–2827.

Bascou, J., Tommasi, A. & Mainprice, D. (2002). Plastic deformation and development of clinopyroxene lattice preferred orientations in eclogites. *Journal of Structural Geology* **24**, 1357–1368.

Bauer, P., Palm, S. & Handy, M. R. (2000). Strain localization and fluid pathways in mylonite: inferences from *in situ* deformation of a water-bearing quartz analogue (norcamphor). *Tectonophysics* **320**, 141–165.

Bell, D. R., Ihinger, P. D. & Rossman, G. R. (1995). Quantitative analysis of trace OH in garnet and pyroxenes. *American Mineralogist* **80**, 465–474.

Ben Ismail, W. & Mainprice, D. (1998). An olivine fabric database: an overview of upper mantle fabrics and seismic anisotropy. *Tectonophysics* **296**, 145–157.

Bercovici, D. & Ricard, Y. (2012). Mechanisms for the generation of plate tectonics by two-phase grain-damage and pinning. *Physics of the Earth and Planetary Interiors* **202–203**, 27–55.

Blacic, J. D. & Christie, J. M. (1984). Plasticity and hydrolytic weakening of quartz single crystals. *Journal of Geophysical Research* **89**, 4223–4239.

Bodinier, J. L., Garrido, C. J., Chanefo, I., Bruguier, O. & Gervilla, F. (2008). Origin of pyroxenite–peridotite veined mantle by refertilization reactions: Evidence from the Ronda peridotite (Southern Spain). *Journal of Petrology* **49**, 999–1025.

Borghini, G., Fumagalli, P. & Rampone, E. (2010). The stability of plagioclase in the upper mantle: subsolidus experiments on fertile and depleted lherzolite. *Journal of Petrology* **51**, 229–254.

Borghini, G., Fumagalli, P. & Rampone, E. (2011). The geobarometric significance of plagioclase in mantle peridotites: A link between nature and experiments. *Lithos* **126**, 42–53.

Botcharnikov, R., Freise, M., Holtz, F. & Behrens, H. (2005). Solubility of C–O–H mixtures in natural melts: new experimental data and application range of recent models. *Annals of Geophysics* **48**, 633–646.

Boudier, F., Ceuleneer, G. & Nicolas, A. (1988). Shear zones, thrusts and related magmatism in the Oman ophiolite—initiation of thrusting on an oceanic ridge. *Tectonophysics* **151**, 275–296.

Braun, J., Chéry, J., Poliakov, A., Mainprice, D., Vauchez, A., Tomassi, A. & Daigniéres, M. (1999). A simple parameterization of strain localization in the ductile regime due to grain size reduction: A case study for olivine. *Journal of Geophysical Research* **104**, 25167–25181.

Brey, G. P. & Köhler, T. P. (1990). Geothermobarometry in four phase lherzolites II. New thermobarometers and practical assessment of existing thermobarometers. *Journal of Petrology* **31**, 1353–1378.

Brodie, K. H. (1980). Variations in mineral chemistry across a shear zone in phlogopite peridotite. *Journal of Structural Geology* **2**, 265–272.

Bunge, H. J. (1982). *Texture Analysis in Materials Sciences*. Butterworth.

Burg, J.-P. & Vigneresse, J.-L. (2002). Non-linear feedback loops in the rheology of cooling–crystallizing felsic magma and heating–melting felsic rock. In: De Meer, S., Drury, M. R., De Bresser, J. H. P. & Pennock, G. (eds) *Deformation Mechanisms, Rheology and Tectonics: Current Status and Future Perspectives. Geological Society, London, Special Publications* **200**, 275–292.

Bürgmann, R. & Dresen, G. (2008). Rheology of the lower crust and upper mantle: evidence from rock mechanics, geodesy, and field observations. *Annual Review of Earth and Planetary Sciences* **36**, 531–567.

Bystricky, M. & Mackwell, S. (2001). Creep of dry clinopyroxene aggregates. *Journal of Geophysical Research* **106**, 13443–13454.

Carter, N. & Avé-Lallemant, H. (1970). High temperature flow of dunite and peridotite. *Geological Society of America Bulletin* **81**, 2181–2202.

Chen, J., Inoue, T., Weidner, D. J., Wu, Y. & Vaughan, M. T. (1998). Strength and water weakening of mantle minerals, olivine, wadsleyite and ringwoodite. *Geophysical Research Letters* **25**, 575–578.

Chen, S., Hiraga, T. & Kohlstedt, D. L. (2006). Water weakening of clinopyroxene in the dislocation creep regime. *Journal of Geophysical Research* **111**, doi: 10.1029/2005JB003885.

Chopra, P. N. & Paterson, M. S. (1984). The role of water in the deformation of dunite. *Journal of Geophysical Research* **89**, 7861–7876.

Connolly, J. A. D. (2009). The geodynamic equation of state: What and how. *Geochemistry, Geophysics, Geosystems* **10**, doi: 10.1029/2009GC002540.

Dale, J., Holland, T. & Powell, R. (2000). Hornblende–garnet–plagioclase thermobarometry: a natural assemblage calibration of the thermodynamics of hornblende. *Contributions to Mineralogy and Petrology* **140**, 353–362.

Dale, J., Powell, R., White, R. W., Elmer, F. L. & Holland, T. J. B. (2005). A thermodynamic model for Ca–Na clinoamphiboles in Na_2O–CaO–FeO–MgO–Al_2O_3–SiO_2–H_2O–O for petrological calculations. *Journal of Metamorphic Geology* **23**, 771–791.

Darot, M. (1973). Méthodes d'analyse structurale et cinématique. Application à l'étude du massif ultrabasique de la Sierra Bermeja. University of Nantes, Ph.D. thesis, 120 p.

De Bresser, J. H. P., Ter Heege, J. H. & Spiers, C. J. (2001). Grain size reduction by dynamic recrystallization: can it result in major rheological weakening? *International Journal of Earth Sciences* **90**, 28–45.

Della Ventura, G., Hawthorne, F. C., Robert, J.-L. & Iezzi, G. (2003). Synthesis and infrared spectroscopy of amphiboles along the tremolite–pargasite join. *European Journal of Mineralogy* **15**, 341–347.

Demouchy, S., Tommasi, A., Barou, F., Mainprice, D. & Cordier, P. (2012). Deformation of olivine in torsion under hydrous conditions. *Physics of the Earth and Planetary Interiors* **202–203**, 56–70.

de Ronde, A. A., Heilbronner, R., Stunitz, H. & Tullis, J. (2004). Spatial correlation of deformation and mineral reaction in experimentally deformed plagioclase–olivine aggregates. *Tectonophysics* **389**, 93–109.

Diener, J. F. A. & Powell, R. (2012). Revised activity–composition models for clinopyroxene and amphibole. *Journal of Metamorphic Geology* **30**, 131–142.

Diener, J. F. A., Powell, R., White, R. W. & Holland, T. J. B. (2007). A new thermodynamic model for clino- and orthoamphiboles in the system Na_2O–CaO–FeO–MgO–Al_2O_3–SiO_2–H_2O–O. *Journal of Metamorphic Geology* **25**, 631–656.

Drury, M. R., Vissers, R. L. M., van der Wal, D. & Hoogerduijn Strating, E. H. (1991). Shear localisation in upper mantle peridotites. *Pure and Applied Geophysics* **137**, 439–460.

Etheridge, M. A. & Wilkie, J. C. (1979). Grainsize reduction, grain boundary sliding and the flow strength of mylonites. *Tectonophysics* **58**, 159–178.

Etheridge, M. A., Wall, V. J. & Vernon, R. H. (1983). The role of the fluid phase during regional metamorphism and deformation. *Journal of Metamorphic Geology* **1**, 205–226.

Falloon, T. J. & Green, D. H. (1987). Anhydrous partial melting of MORB pyrolite and other peridotite compositions at 10 kbar: Implications for the origin of primitive MORB glasses. *Mineralogy and Petrology* **37**, 181–219.

Fliervoet, T. F. & White, S. H. (1995). Quartz deformation in a very fine grained quartzo-feldspathic mylonite: a lack of evidence for dominant grain boundary sliding deformation. *Journal of Structural Geology* **17**, 1095–1109.

Frets, E., Tommasi, A., Garrido, C. J., Padrón-Navarta, J. A., Amri, I. & Targuisti, K. (2012). Deformation processes and rheology of pyroxenites under lithospheric mantle conditions. *Journal of Structural Geology* **39**, 138–157.

Furusho, M. & Kanagawa, K. (1999). Transformation-induced strain localization in a lherzolite mylonite from the Hidaka metamorphic belt of central Hokkaido, Japan. *Tectonophysics* **313**, 411–432.

Garrido, C. J. & Bodinier, J. L. (1999). Diversity of mafic rocks in the Ronda peridotite: Evidence for pervasive melt–rock reaction during heating of subcontinental lithosphere by upwelling asthenosphere. *Journal of Petrology* **40**, 729–754.

Garrido, C. J., Gueydan, F., Booth-Rea, G., Precigout, J., Hidas, K., Padron-Navarta, J. A. & Marchesi, C. (2011). Garnet lherzolite and garnet–spinel mylonite in the Ronda peridotite: Vestiges of Oligocene backarc mantle lithospheric extension in the western Mediterranean. *Geology* **39**, 927–930.

Gasparik, T. (1984). Two-pyroxene thermobarometry with new experimental data in the system CaO–MgO–Al_2O_3–SiO_2. *Contributions to Mineralogy and Petrology* **87**, 87–97.

Gasparik, T. (1987). Orthopyroxene thermobarometry in simple and complex systems. *Contributions to Mineralogy and Petrology* **96**, 357–370.

Gavrilenko, P. (2008). Water solubility in diopside. University of Bayreuth, Ph.D. thesis, 144 p.

Gavrilenko, P. & Keppler, H. (2007). Water solubility in clinopyroxene. *Geochimica et Cosmochimica Acta* **71**, A312–A312.

Gervilla, F., Padrón-Navarta, J. A., Kerestedjian, T., Sergeeva, I., González-Jiménez, J. M. & Fanlo, I. (2012). Formation of ferrian chromite in podiform chromitites from the Golyamo Kamenyane serpentinite, Eastern Rhodopes, SE Bulgaria: a two-stage process. *Contributions to Mineralogy and Petrology* **164**, 643–657.

Green, D. H. & Hibberson, W. (1970). The instability of plagioclase in peridotite at high pressure. *Lithos* **3**, 209–221.

Handy, M. R. (1989). Deformation regimes and the rheological evolution of fault zones in the lithosphere: the effects of pressure, temperature, grainsize and time. *Tectonophysics* **163**, 119–152.

Handy, M. R., Wissing, S. B. & Streit, L. E. (1999). Frictional–viscous flow in mylonite with varied bimineralic composition and its effect on lithospheric strength. *Tectonophysics* **303**, 175–191.

Hansen, L. N., Zimmerman, M. E., Dillman, A. M. & Kohlstedt, D. L. (2012). Strain localization in olivine aggregates at high temperature: A laboratory comparison of constant-strain-rate and constant-stress boundary conditions. *Earth and Planetary Science Letters* **333–334**, 134–145.

Hart, S. R. & Zindler, A. (1986). In search of a bulk-Earth composition. *Chemical Geology* **57**, 247–267.

Herzberg, C. T. (1972). Stability fields of plagioclase- and spinel lherzolite. *Progress in Experimental Petrology* **2**, 145–148.

Hidas, K., Guzmics, T., Szabo, C., Kovacs, I., Bodnar, R. J., Zajacz, Z., Nedli, Z., Vaccari, L. & Perucchi, A. (2010). Coexisting silicate melt inclusions and H_2O-bearing, CO_2-rich fluid inclusions in mantle peridotite xenoliths from the Carpathian–Pannonian region (central Hungary). *Chemical Geology* **274**, 1–18.

Hidas, K., Booth-Rea, G., Garrido, C. J., Martinez-Martinez, J. M., Padron-Navarta, J. A., Konc, Z., Giaconia, F., Frets, E. & Marchesi, C. (2013). Backarc basin inversion and subcontinental mantle emplacement in the crust: kilometre-scale folding and shearing at the base of the proto-Alborán lithospheric mantle (Betic Cordillera, southern Spain). *Journal of the Geological Society, London* **170**, 47–55.

Hier-Majumder, S., Mei, S. & Kohlstedt, D. L. (2005). Water weakening of clinopyroxenite in diffusion creep. *Journal of Geophysical Research* **110**, doi: 10.1029/2004JB003414.

Hirose, K. & Kushiro, I. (1993). Partial melting of dry peridotites at high pressures: Determination of compositions of melts segregated from peridotite using aggregates of diamond. *Earth and Planetary Science Letters* **114**, 477–489.

Hirschmann, M. & Kohlstedt, D. (2012). Water in Earth's mantle. *Physics Today* **65**, 40–45.

Hirth, G. & Kohlstedt, D. L. (1996). Water in the oceanic upper mantle: Implications for rheology, melt extraction and the evolution of the lithosphere. *Earth and Planetary Science Letters* **144**, 93–108.

Hirth, G. & Kohlstedt, D. (2003). Rheology of the upper mantle and the mantle wedge: a view from the experimentalists. In: Eiler, J. M. (ed.) *Inside the Subduction Factory. Geophysical Monograph, American Geophysical Union* **138**, 83–105.

Holland, T. & Powell, R. (1996). Thermodynamics of order–disorder in minerals. 2. Symmetric formalism applied to solid solutions. *American Mineralogist* **81**, 1425–1437.

Holland, T. J. B., Baker, J. & Powell, R. (1998). Mixing properties and activity-composition relationships of chlorites in the system MgO-FeO-Al_2O_3-SiO_2-H_2O. *European Journal of Mineralogy* **10**, 395–406.

Jaroslow, G. E., Hirth, G. & Dick, H. J. B. (1996). Abyssal peridotite mylonites: implications for grain-size sensitive flow and strain localization in the oceanic lithosphere. *Tectonophysics* **256**, 17–37.

Ji, S. & Xia, B. (2002). *Rheology of Polyphase Earth Materials*. Polytechnic International Press.

Jin, D., Karato, S.-i. & Obata, M. (1998). Mechanisms of shear localization in the continental lithosphere: inference from the deformation microstructures of peridotites from the Ivrea zone, northwestern Italy. *Journal of Structural Geology* **20**, 195–209.

Johnson, E. A. (2003). Hydrogen in nominally anhydrous crustal minerals, California Institute of Technology, Ph.D. thesis, 305.

Johnson, E. A. & Rossman, G. R. (2003). The concentration and speciation of hydrogen in feldspars using FTIR and ^{1}H MAS NMR spectroscopy. *American Mineralogist* **88**, 901–911.

Johnson, E. A. & Rossman, G. R. (2004). A survey of hydrous species and concentrations in igneous feldspars. *American Mineralogist* **89**, 586–600.

Jung, H. & Karato, S.-I. (2001). Water-induced fabric transitions in olivine. *Science* **293**, 1460–1463.

Kaczmarek, M.-A. & Tommasi, A. (2011). Anatomy of an extensional shear zone in the mantle, Lanzo massif, Italy. *Geochemistry, Geophysics, Geosystems* **12**, Q0AG06.

Karato, S.-i. (2008). *Deformation of Earth Materials: an Introduction to the Rheology of Solid Earth*. Cambridge University Press.

Karato, S.-i. & Jung, H. (2003). Effects of pressure on high-temperature dislocation creep in olivine. *Philosophical Magazine* **83**, 401–414.

King, P. L. & Holloway, J. R. (2002). CO_2 solubility and speciation in intermediate (andesitic) melts: the role of H_2O and composition. *Geochimica et Cosmochimica Acta* **66**, 1627–1640.

Kirby, S. H. (1985). Rock mechanics observations pertinent to the rheology of the continental lithosphere and the localization of strain along shear zones. *Tectonophysics* **119**, 1–27.

Klemme, S., Ivanic, T. J., Connolly, J. A. D. & Harte, B. (2009). Thermodynamic modelling of Cr-bearing garnets with implications for diamond inclusions and peridotite xenoliths. *Lithos* **112(Supplement 2)**, 986–991.

Kohlstedt, D. L. (2006). The role of water in high-temperature rock deformation. In: Keppler, H. & Smyth, J. R. (eds) *Water in Nominally Anhydrous Minerals. Mineralogical Society of America and Geochemical Society, Reviews in Mineralogy and Geochemistry* **62**, 377–396.

Kovács, I., Hermann, J., O'Neill, H. S. C., Gerald, J. F., Sambridge, M. & Horváth, G. (2008). Quantitative absorbance spectroscopy with unpolarized light: Part II. Experimental evaluation and development of a protocol for quantitative analysis of mineral IR spectra. *American Mineralogist* **93**, 765–778.

Lawlis, J. D., Zhao, Y. H. & Karato, S. (2001). High-temperature creep in a Ni_2GeO_4: a contribution to creep systematics in spinel. *Physics and Chemistry of Minerals* **28**, 557–571.

Lenoir, X., Garrido, C. J., Bodinier, J. L., Dautria, J. M. & Gervilla, F. (2001). The recrystallization front of the Ronda peridotite: Evidence for melting and thermal erosion of subcontinental lithospheric mantle beneath the Alboran basin. *Journal of Petrology* **42**, 141–158.

Lloyd, G. E. (2004). Microstructural evolution in a mylonitic quartz simple shear zone: the significant roles of dauphine twinning and misorientation. In: Alsop, G. I., Holdsworth, R. E., McCaffrey, K. J. W. & Hand, M. (eds) *Flow Processes in Faults and Shear Zones. Geological Society, London, Special Publications* **224**, 39–61.

Lloyd, G. E., Farmer, A. B. & Mainprice, D. (1997). Misorientation analysis and the formation and orientation of subgrain and grain boundaries. *Tectonophysics* **279**, 55–78.

Mackwell, S. J., Kohlstedt, D. L. & Paterson, M. S. (1985). The role of water in the deformation of olivine single-crystals. *Journal of Geophysical Research—Solid Earth and Planets* **90**, 1319–1333.

Mahan, K. H., Goncalves, P., Williams, M. L. & Jercinovic, M. J. (2006). Dating metamorphic reactions and fluid flow: application to exhumation of high-*P* granulites in a crustal-scale shear zone, western Canadian Shield. *Journal of Metamorphic Geology* **24**, 193–217.

Matsyuk, S. S. & Langer, K. (2004). Hydroxyl in olivines from mantle xenoliths in kimberlites of the Siberian platform. *Contributions to Mineralogy and Petrology* **147**, 413–437.

McDonough, W. F. & Sun, S. S. (1995). The composition of the Earth. *Chemical Geology* **120**, 223–253.

Mierdel, K., Keppler, H., Smyth, J. R. & Langenhorst, F. (2007). Water solubility in aluminous orthopyroxene and the origin of Earth's asthenosphere. *Science* **315**, 364–368.

Molli, G., Conti, P., Giorgetti, G., Meccheri, M. & Oesterling, N. (2000). Microfabric study on the deformational and thermal history of the Alpi Apuane marbles (Carrara marbles), Italy. *Journal of Structural Geology* **22**, 1809–1825.

Neves, S. P., Tommasi, A., Vauchez, A. & Hassani, R. (2008). Intraplate continental deformation: Influence of a heat-producing layer in the lithospheric mantle. *Earth and Planetary Science Letters* **274**, 392–400.

Newman, J., Lamb, W. M., Drury, M. R. & Vissers, R. L. M. (1999). Deformation processes in a peridotite shear zone: reaction-softening by an H_2O-deficient, continuous net transfer reaction. *Tectonophysics* **303**, 193–222.

Newton, R. C., Charlu, T. V. & Kleppa, O. J. (1980). Thermochemistry of the high structural state plagioclases. *Geochimica et Cosmochimica Acta* **44**, 933–941.

Nimis, P. & Grütter, H. (2010). Internally consistent geothermometers for garnet peridotites and pyroxenites. *Contributions to Mineralogy and Petrology* **159**, 411–427.

Obata, M. (1980). The Ronda peridotite—garnet-lherzolite, spinel-lherzolite, and plagioclase-lherzolite facies and the *P–T* trajectories of a high-temperature mantle intrusion. *Journal of Petrology* **21**, 533–572.

Ogawa, M. (1987). Shear instability in a viscoelastic material as the cause of deep focus earthquakes. *Journal of Geophysical Research* **92**, 13801–13810.

Oliver, N. H. S. (1996). Review and classification of structural controls on fluid flow during regional metamorphism. *Journal of Metamorphic Geology* **14**, 477–492.

Ozawa, K. (1989). Stress-induced Al–Cr zoning of spinel in deformed peridotites. *Nature* **338**, 141–144.

Perkins, D. & Anthony, E. Y. (2011). The evolution of spinel lherzolite xenoliths and the nature of the mantle at Kilbourne Hole, New Mexico. *Contributions to Mineralogy and Petrology* **162**, 1139–1157.

Peslier, A. H., Luhr, J. F. & Post, J. (2002). Low water contents in pyroxenes from spinel-peridotites of the oxidized, sub-arc mantle wedge. *Earth and Planetary Science Letters* **201**, 69–86.

Platt, J. P. & Behr, W. M. (2011). Grainsize evolution in ductile shear zones: Implications for strain localization and the strength of the lithosphere. *Journal of Structural Geology* **33**, 537–550.

Poirier, J. P. (1980). Shear localization and shear instability in materials in the ductile field. *Journal of Structural Geology* **2**, 135–142.

Poirier, J. P. & Nicolas, A. (1975). Deformation-induced recrystallization due to progressive misorientation of subgrains, with special reference to mantle peridotites. *Journal of Geology* **83**, 707–720.

Powell, R. & Holland, T. (1999). Relating formulations of the thermodynamics of mineral solid solutions: Activity modeling of pyroxenes, amphiboles, and micas. *American Mineralogist* **84**, 1–14.

Precigout, J., Gueydan, F., Gapais, D., Garrido, C. J. & Essaifi, A. (2007). Strain localisation in the subcontinental mantle—a ductile alternative to the brittle mantle. *Tectonophysics* **445**, 318–336.

Presnall, D. C. (1976). Alumina content of enstatite as a geobarometer for plagioclase and spinel lherzolites. *American Mineralogist* **61**, 582–588.

Randle, V. (1993). *The Measurement of Grain Boundary Geometry*. Bristol: Institute of Physics.

Regenauer-Lieb, K., Yuen, D. A. & Branlund, J. (2001). The initiation of subduction: Criticality by addition of water? *Science* **294**, 578–580.

Roedder, E. (1992). Fluid inclusion evidence for immiscibility in magmatic differentiation. *Geochimica et Cosmochimica Acta* **56**, 5–20.

Rozel, A., Ricard, Y. & Bercovici, D. (2011). A thermodynamically self-consistent damage equation for grain size evolution during dynamic recrystallization. *Geophysical Journal International* **184**, 719–728.

Rubie, D. C. (1986). The catalysis of mineral reactions by water and restrictions on the presence of aqueous fluid during metamorphism. *Mineralogical Magazine* **50**, 399–415.

Rutter, E. H. & Brodie, K. H. (1988). The role of tectonic grain size reduction in the rheological stratification of the lithosphere. *Geologische Rundschau* **77**, 295–307.

Rybacki, E. & Dresen, G. (2004). Deformation mechanism maps for feldspar rocks. *Tectonophysics* **382**, 173–187.

Rybacki, E., Gottschalk, M., Wirth, R. & Dresen, G. (2006). Influence of water fugacity and activation volume on the flow properties of fine-grained anorthite aggregates. *Journal of Geophysical Research* **111**, doi: 10.1029/2005JB003663.

Sambridge, M., Gerald, J. F., Kovacs, I., O'Neill, H. S. C. & Hermann, J. (2008). Quantitative absorbance spectroscopy with unpolarized light: Part I. Physical and mathematical development. *American Mineralogist* **93**, 751–764.

Schmädicke, E. (2000). Phase relations in peridotitic and pyroxenitic rocks in the model systems CMASH and NCMASH. *Journal of Petrology* **41**, 69–86.

Schmid, S. M. (1982). Microfabric studies as indicators of deformation mechanisms and flow laws operative in mountain building. In: Hsü, K. J. (ed.) *Mountain Building Processes*. Academic Press, pp. 95–110.

Selverstone, J., Morteani, G. & Staude, J. M. (1991). Fluid channelling during ductile shearing: transformation of granodiorite into aluminous schist in the Tauern Window, Eastern Alps. *Journal of Metamorphic Geology* **9**, 419–431.

Shimizu, I. (2008). Theories and applicability of grain size piezometers: The role of dynamic recrystallization mechanisms. *Journal of Structural Geology* **30**, 899–917.

Sibson, R. H. (1977). Fault rocks and fault mechanisms. *Journal of the Geological Society, London* **133**, 191–213.

Skemer, P., Warren, J. M., Kelemen, P. B. & Hirth, G. (2010). Microstructural and rheological evolution of a mantle shear zone. *Journal of Petrology* **51**, 43–53.

Skogby, H. (2006). Water in natural mantle minerals I: Pyroxenes. In: Keppler, H. & Smyth, J. R. (eds) *Water in Nominally Anhydrous Minerals. Mineralogical Society of America and Geochemical Society, Reviews in Mineralogy and Geochemistry* **62**, 155–167.

Soustelle, V., Tommasi, A., Bodinier, J. L., Garrido, C. J. & Vauchez, A. (2009). Deformation and reactive melt transport in the mantle lithosphere above a large-scale partial melting domain: the Ronda Peridotite Massif, southern Spain. *Journal of Petrology* **50**, 1235–1266.

Soustelle, V., Tommasi, A., Demouchy, S. & Ionov, D. A. (2010). Deformation and fluid–rock interaction in the supra-subduction mantle: microstructures and water contents in peridotite xenoliths from the Avacha Volcano, Kamchatka. *Journal of Petrology* **51**, 363–394.

Stünitz, H. & Tullis, J. (2001). Weakening and strain localization produced by syn-deformational reaction of plagioclase. *International Journal of Earth Sciences* **90**, 136–148.

Tarantola, A. & Valette, B. (1982). Generalized nonlinear inverse problems solved using the least squares criterion. *Reviews of Geophysics* **20**, 219–232.

Taylor, W. R. (1998). An experimental test of some geothermometer and geobarometer formulations for upper mantle peridotites with application to the thermobarometry of fertile lherzolite and garnet websterite. *Neues Jahrbuch für Mineralogie, Abhandlungen* **172**, 381–408.

Ter Heege, J. H., De Bresser, J. H. P. & Spiers, C. J. (2002). The influence of dynamic recrystallization on the grain size distribution and rheological behaviour of Carrara marble deformed in axial compression. In: De Meer, S., Drury, M. R., De Bresser, J. H. P. & Pennock, G. (eds) *Deformation Mechanisms, Rheology and Tectonics: Current Status and Future Perspectives. Geological Society, London, Special Publications* **200**, 331–353.

Thielmann, M. & Kaus, B. J. P. (2012). Shear heating induced lithospheric-scale localization: Does it result in subduction? *Earth and Planetary Science Letters* **359–360**, 1–13.

Tommasi, A. & Vauchez, A. (2001). Continental rifting parallel to ancient collisional belts: an effect of the mechanical anisotropy of the lithospheric mantle. *Earth and Planetary Science Letters* **185**, 199–210.

Tommasi, A., Vauchez, A. & Daudre, B. (1995). Initiation and propagation of shear zones in a heterogeneous continental lithosphere. *Journal of Geophysical Research—Solid Earth* **100**, 22083–22101.

Tommasi, A., Tikoff, B. & Vauchez, A. (1999). Upper mantle tectonics: three-dimensional deformation, olivine crystallographic fabrics and seismic properties. *Earth and Planetary Science Letters* **168**, 173–186.

Tommasi, A., Mainprice, D., Canova, G. & Chastel, Y. (2000). Viscoplastic self-consistent and equilibrium-based modeling of olivine lattice preferred orientations: Implications for the upper mantle seismic anisotropy. *Journal of Geophysical Research—Solid Earth* **105**, 7893–7908.

Tommasi, A., Knoll, M., Vauchez, A., Signorelli, J., Thoraval, C. & Loge, R. (2009). Structural reactivation in plate tectonics controlled by olivine crystal anisotropy. *Nature Geoscience* **2**, 422–426.

Torres-Roldán, R. L., García-Casco, A. & García-Sánchez, P. A. (2000). CSpace: an integrated workplace for the graphical and algebraic analysis of phase assemblages on 32-bit wintel platforms. *Computers & Geosciences* **26**, 779–793.

Toy, V. G., Newman, J., Lamb, W. & Tikoff, B. (2010). The role of pyroxenites in formation of shear instabilities in the mantle: evidence from an ultramafic ultramylonite, Twin Sisters Massif, Washington. *Journal of Petrology* **51**, 55–80.

Treagus, S. H. & Sokoutis, D. (1992). Laboratory modelling of strain variation across rheological boundaries. *Journal of Structural Geology* **14**, 405–424.

Tullis, J. & Yund, R. A. (1985). Dynamic recrystallization of feldspar: A mechanism for ductile shear zone formation. *Geology* **13**, 238–241.

Twiss, R. (1977). Theory and applicability of recrystallized grain size paleopiezometer. *Pure and Applied Geophysics* **115**, 227–244.

Twiss, R. & Sellars, C. M. (1978). Limits of applicability of the recrystallized grain size geopiezometer. *Geophysical Research Letters* **5**, 337–340.

Van der Wal, D. & Bodinier, J. L. (1996). Origin of the recrystallisation front in the Ronda peridotite by km-scale pervasive porous melt flow. *Contributions to Mineralogy and Petrology* **122**, 387–405.

Van der Wal, D. & Vissers, R. L. M. (1996). Structural petrology of the Ronda peridotite, SW Spain: deformation history. *Journal of Petrology* **37**, 23–43.

Vauchez, A. & Garrido, C. J. (2001). Seismic properties of an asthenospherized lithospheric mantle: constraints from lattice preferred orientations in peridotite from the Ronda massif. *Earth and Planetary Science Letters* **192**, 235–249.

Vauchez, A., Tommasi, A. & Mainprice, D. (2012). Faults (shear zones) in the Earth's mantle. *Tectonophysics* **558–559**, 1–27.

Vigneresse, J. L. & Burg, J. P. (2004). Strain-rate-dependent rheology of partially molten rocks. In: Grocott, J., McCaffrey, K. J. W., Taylor, G. & Tikoff, B. (eds) *Vertical Coupling and Decoupling in the Lithosphere. Geological Society, London, Special Publications* **227**, 327–336.

Vilotte, J. P., Daignieres, M., Madariaga, R. & Zienkiewicz, O. C. (1984). The role of a heterogeneous inclusion during continental collision. *Physics of the Earth and Planetary Interiors* **36**, 236–259.

Vollmer, F. W. (1990). An application of eigenvalue methods to structural domain analysis. *Geological Society of America Bulletin* **102**, 786–791.

Warren, J. M. & Hirth, G. (2006). Grain size sensitive deformation mechanisms in naturally deformed peridotites. *Earth and Planetary Science Letters* **248**, 438–450.

Wheeler, J., Prior, D., Jiang, Z., Spiess, R. & Trimby, P. (2001). The petrological significance of misorientations between grains. *Contributions to Mineralogy and Petrology* **141**, 109–124.

Witt-Eickschen, G. & Seck, H. A. (1991). Solubility of Ca and Al in orthopyroxene from spinel peridotite—an improved version of an empirical geothermometer. *Contributions to Mineralogy and Petrology* **106**, 431–439.

Zeh, A., Holland, T. J. B. & Klemd, R. (2005). Phase relationships in grunerite–garnet-bearing amphibolites in the system CFMASH, with applications to metamorphic rocks from the Central Zone of the Limpopo Belt, South Africa. *Journal of Metamorphic Geology* **23**, 1–17.

APPENDIX A: PERPLE.X

Theoretical considerations for simplifying the system

The full system Cr_2O_3–MnO–Na_2O–CaO–FeO–MgO–Al_2O_3–SiO_2–H_2O (CrMnNCFMASH) can be reduced to the NCMASH system after projection from the $MgFe_{-1}$, $FeMn_{-1}$, $AlCr_{-2}$ exchange vectors without significant limitations. In this latter model system all subsamples have virtually the same composition. A noteworthy change in the Tschermaks content in pyroxene is associated with the deformation and it is illustrated in ACS (Al_2O_3–CaO–SiO_2) projected diagrams in Fig. 9a–c. Pyroxenes from the coarse-grained Spl websterite are rich in Tschermaks content and show minor core and rim variations (Fig. 9a). Core and rim compositions also overlap in the mylonite but in this case the pyroxene compositions are close to the Al-free end-members (Fig. 9c). Pyroxenes from the protomylonite span the whole compositional range (Fig. 9b), pointing to a continuous readjustment of the pyroxene composition during deformation.

Subsolidus phase relations for protomylonite (RK139-5T) (Fig. 9d) have been computed in the NCMASH system with Perple_X (Connolly, 2009), and the updated internally consistent thermodynamic dataset of Holland & Powell (1998, updated in 2002). Some additional calculations in more complex systems were computed to establish the suitability of the results in the NCMASH system. Solid solution models included in this system were clinopyroxene (diopside–CaTschermaks–jadeite, Holland & Powell, 1996; modified for non-ideal CaTschermaks by Zeh *et al.*, 2005), orthopyroxene (enstatite–MgTschermaks, Powell & Holland, 1999), garnet (grossular–pyrope, Holland & Powell, 1998), amphibole (pargasite–tremolite–tschermakite–glaucophane, Dale *et al.*, 2005), chlorite (clinochlore–amesite, Holland *et al.*, 1998) and plagioclase (albite–anorthite, Newton *et al.*, 1980).

Justification of *P–T* estimates in the iron-free system

It is well established that the consideration of other components such as FeO lowers the upper pressure limit of the spinel stability field (e.g. Perkins & Anthony, 2011). Our own computations indicate that in the iron-bearing system this pressure limit is lowered to *c.* 1·0 GPa for the same temperature but is then increased to 1·8 GPa if FeO and Cr_2O_3 are both included, or to 2·0 GPa if Cr_2O_3 is considered only as an extra component. The preference for a simplified model not including FeO is justified here because Fe–Mg partitioning has little effect on the pressure stability field of plagioclase [see Borghini *et al.* (2010) for a comprehensive discussion], which is the field specifically addressed in this study. Furthermore, it has been noted that if Cr_2O_3 is considered in addition to FeO the upper pressure limit for the plagioclase stability field is unrealistically lowered to 0·2 GPa at 1000°C, which is experimentally unsupported (Borghini *et al.*, 2010). The inability of the spinel solid solution (Klemme *et al.*, 2009) to handle both Fe–Mg and Al–Cr substitutions was also suggested by Gervilla *et al.* (2012). Although Al–Cr partitioning has been proven to modify to some extent the upper pressure stability field of plagioclase, this effect is not great (*c.* 0·08 GPa lower in the Cr-NCMASH compared with the NCMASH system at 1000°C based on our own calculations) and therefore it is not considered in this study.

However, it is worth noting that if Cr_2O_3 alone is included as an extra component a Cr-rich spinel is stable in the plagioclase stability field, as indicated by Borghini *et al.* (2010), which is inconsistent with the persistence of Cr-poor spinel porphyroclasts in the mylonites reported here.

Stability of amphibole

Because of the implications for the possible stability of amphibole during deformation in the studied samples all available amphibole solid solutions were tested to check the consistency of the Dale *et al.* (2005) model. This model results in the coexistence of two amphiboles at temperatures lower than 750°C, corresponding to orthopyroxene-free assemblages (fields marked with asterisk in Fig. 9d). Comparable amphibole stability limits are obtained if pure pargasite and tremolite are considered. The same immiscibility gap is also noticed in the more updated version of the amphibole solid solution by Diener *et al.* (2007) and Diener & Powell (2012). In this latter model the highest amphibole thermal stability is displaced to some extent (from 1050 to 1000°C at *c.* 0·8 GPa). Interestingly, previous model solutions such as that of Dale *et al.* (2000) do not show immiscibility at low temperature. However, the presence of this immiscibility is of little relevance in this study.

APPENDIX B: NUMERICAL MODELING

Numerical experiments

We conducted 1D numerical experiments to constrain the rheology of the system, summarized in Tables 4 and 5. In simple shear deformation it is described by the following partial differential equation (τ and x denote shear stress and spatial coordinate respectively):

$$\frac{\partial \tau}{\partial x} = 0 \tag{S1}$$

which implies that the stress in the whole system is constant. We additionally assume that deformation is purely viscous and that the rheology is governed by dislocation and diffusion creep. The strain rates of both mechanisms are given by (e.g. Hirth & Kohlstedt, 2003)

$$\dot{\varepsilon}_{\mathrm{dis}} = A_{\mathrm{dis}} \tau^{n_{\mathrm{dis}}} \exp \frac{E_{\mathrm{a,dis}} + V_{\mathrm{a,dis}} P}{RT} \tag{S2}$$

$$\dot{\varepsilon}_{\mathrm{dif}} = A_{\mathrm{dif}} \tau d^{-m_{\mathrm{dif}}} \exp \frac{E_{\mathrm{a,dif}} + V_{\mathrm{a,dif}} P}{RT}. \tag{S3}$$

A, n, m, E_{a} and V_{a} are the pre-exponential constant, stress exponent (dislocation creep only), grain-size exponent (diffusion creep only), activation energy and activation volume (the different deformation mechanisms are denoted by the respective indices). T, d, P and R are temperature, grain size, pressure and the gas constant.

The total strain rate is then given by the sum of both strain rates:

$$\varepsilon = \dot{\varepsilon}_{\mathrm{dis}} + \dot{\varepsilon}_{\mathrm{dif}}. \tag{S4}$$

To account for the polymineralic nature of the modeled rock, we averaged the rheological properties of the different minerals in each element. The upper and lower bounds of such an average are given by the isostress (Voigt bound) and the isostrainrate (Reuss bound) averages respectively and result in expressions for the average rheological properties of the composite material (Ji & Xia, 2002):

$$n_{\mathrm{u}} = \sum_{i=1}^{N} \phi_i n_i \tag{S5}$$

$$m_{\mathrm{u}} = \sum_{i=1}^{N} \phi_i m_i \tag{S6}$$

$$A_{\mathrm{u}} = \prod_{i=1}^{N} \left(\frac{A_i}{\alpha_i} \right)^{\phi_i} \tag{S7}$$

$$E_{\mathrm{a,u}} = \sum_{i=1}^{N} \phi_i E_{\mathrm{a},i} \tag{S8}$$

$$V_{\mathrm{a,u}} = \sum_{i=1}^{N} \phi_i V_{\mathrm{a},i} \tag{S9}$$

and

$$n_{\mathrm{l}} = \frac{1}{\sum_{i=1}^{N} \frac{\phi_i}{n_i}} \tag{S10}$$

$$m_{\mathrm{l}} = n_{\mathrm{l}} \sum_{i=1}^{N} \frac{\phi_i m_i}{n_i} \tag{S11}$$

$$A_{\mathrm{l}} = \prod_{i=1}^{N} \left(\frac{A_i}{\alpha_i^{m_i}} \right)^{n_{\mathrm{l}} \frac{\phi_i}{n_i}} \tag{S12}$$

$$E_{\mathrm{a,l}} = n_{\mathrm{l}} \sum_{i=1}^{N} \frac{\phi_i E_{\mathrm{a},i}}{n_i} \tag{S13}$$

$$V_{\mathrm{a,l}} = n_{\mathrm{l}} \sum_{i=1}^{N} \frac{\phi_i V_{a,i}}{n_i} \tag{S14}$$

with

$$\alpha_i = \frac{d_i}{\sum_{j=1}^{N} \phi_j d_j}. \tag{S15}$$

i and j are summing indices for the different phases, ϕ is their respective volume fraction, the subscript i denotes the volume fraction of the ith phase and the indices u and l denote values for the upper and lower bounds of the averaged rheological parameter.

We then computed the effective rheological parameters (upper and lower bound) for each rock type in our model (for the parameters used in this calculation see Tables 4 and 5). As we did not include any diffusion processes, we can decouple the strain rate computation for each subdomain, thus essentially reducing the 1D model to a 0D model. The strain rate in each subdomain was then computed for a range of temperatures, pressures and stresses according to (S2), (S3) and (S4). It turns out that pressure has a negligible effect on strain rate compared with temperature (as expected). Furthermore, the averaging method does not have a significant effect on the strain rate computation (compared with the effect of hydrated mineral phases in the material).

Finally, we computed the parameter $\beta = \dot{\varepsilon}_{\mathrm{dif}}/\dot{\varepsilon}_{\mathrm{dis}}$ to illustrate the contributions of diffusion and dislocation creep. When $\beta > 1$, diffusion creep is dominant; for $\beta < 1$, dislocation creep is the dominant mechanism.